

CALT-68-2026  
DOE RESEARCH AND  
DEVELOPMENT REPORT

# Color-Octet Quarkonia Production II

Peter Cho<sup>1</sup> and Adam K. Leibovich<sup>2</sup>  
 Lauritsen Laboratory  
 California Institute of Technology  
 Pasadena, CA 91125

## Abstract

We calculate the lowest order hadronic cross sections for producing colored heavy quark-antiquark pairs in  $L = S = 0$  and  $L = S = 1$  configurations. Such  $Q\bar{Q}[{}^1S_0^{(8)}]$  and  $Q\bar{Q}[{}^3P_J^{(8)}]$  states hadronize into  $\psi_Q$  quarkonia at the same order in the NRQCD velocity expansion as previously considered  $Q\bar{Q}[{}^3S_1^{(8)}]$  pairs. Their contributions to prompt Psi and Upsilon production at the Tevatron bring the shapes of theoretical transverse momentum distributions into line with recent CDF measurements. We find that the best fit values for the linear combinations of  $Q\bar{Q}[{}^1S_0^{(8)}]$  and  $Q\bar{Q}[{}^3P_J^{(8)}]$  long distance matrix elements which can be extracted from the data are generally consistent with NRQCD scaling rules.

4/96

---

<sup>1</sup> Work supported in part by a DuBridge Fellowship and by the U.S. Dept. of Energy under DOE Grant no. DE-FG03-92-ER40701.

<sup>2</sup> Work supported in part by the U.S. Dept. of Energy under DOE Grant no. DE-FG03-92-ER40701.

## 1. Introduction

The study of quarkonia has yielded valuable insight into the nature of the strong interaction ever since the discovery of the  $J/\psi$  resonance in 1974. During the past two decades,  $Q\bar{Q}$  bound states have provided useful laboratories for probing both perturbative and nonperturbative aspects of QCD. Recently, investigations of charmonia and bottomonia systems have uncovered some striking surprises. Orders of magnitude disagreements have been found between old predictions and new measurements of Psi and Upsilon production at several collider facilities. These large disparities have called into question the simplest model descriptions of quarkonia and stimulated the development of a new paradigm for treating heavy quark-antiquark systems based upon QCD. Although much theoretical and experimental work remains to be done before a truly consistent picture of quarkonia is established, ongoing studies of these heavy mesons are leading to a better understanding of some basic aspects of strong interaction physics.

Quarkonia bound states are qualitatively different from most other hadrons since they are inherently nonrelativistic. The physics of quarkonia consequently involves several energy scales which are separated by the small velocity  $v$  of the heavy constituents inside  $Q\bar{Q}$  bound states. The most important scales are set by the mass  $M_Q$ , momentum  $M_Q v$  and kinetic energy  $M_Q v^2$  of the heavy quark and antiquark. In order to keep track of this scale hierarchy, an effective field theory called Nonrelativistic Quantum Chromodynamics (NRQCD) has been established [1]. This effective theory for  $Q\bar{Q}$  bound states shares several similarities with the Heavy Quark Effective Theory (HQET) which describes the low energy QCD structure of heavy-light  $Q\bar{q}$  mesons. For example, NRQCD is based upon a double power series expansion in the strong interaction fine structure constant  $\alpha_s = g_s^2/4\pi$  and the velocity parameter  $v \sim 1/\log M_Q$  which is similar to the HQET's double expansion in  $\alpha_s$  and  $1/M_Q$ . Both theories also incorporate approximate spin symmetry relations which constrain various multiplet structures and transition rates. But most importantly, NRQCD systematizes one's understanding of charmonia and bottomonia just as the HQET methodically organizes the physics of  $D$  and  $B$  mesons.

Quarkonia are described within the NRQCD framework in terms of Fock state decompositions. The wavefunction of an S-wave orthoquarkonium vector meson schematically looks like

$$\begin{aligned} |\psi_Q\rangle = & O(1)|Q\bar{Q}[{}^3S_1^{(1)}]\rangle + O(v)|Q\bar{Q}[{}^3P_J^{(8)}]g\rangle \\ & + O(v^2)|Q\bar{Q}[{}^1S_0^{(8)}]g\rangle + O(v^2)|Q\bar{Q}[{}^3S_1^{(1,8)}]gg\rangle + O(v^2)|Q\bar{Q}[{}^3D_J^{(1,8)}]gg\rangle + \dots \end{aligned} \quad (1.1)$$

The spin, orbital and total angular momentum quantum numbers of the  $Q\bar{Q}$  pairs in each Fock component are indicated within the square brackets in spectroscopic notation, while the pairs' color assignments are specified by singlet or octet superscripts. The order in the velocity expansion at which each of these Fock states participates in  $\psi_Q$  annihilation or creation processes is governed by simple NRQCD counting rules [2]. For instance, suppose a heavy quark and antiquark are produced almost on-shell with nearly parallel 3-momenta in some high energy reaction. The low energy hadronization of this pair into a physical  $\psi_Q$  bound state takes place at  $O(v^3)$  if it has the same angular momentum and color quantum numbers as those displayed in the first Fock component of (1.1). The long distance evolution of all other  $Q\bar{Q}$  pairs generated at short distance scales into  $\psi_Q$  mesons occurs at higher orders in the velocity expansion.

If the relative importance of various quarkonia production channels depended solely upon the order in  $v$  at which pairs hadronize into physical bound states, those modes which proceed through the leading Fock components in quarkonia wavefunction decompositions would generally be dominant. This assumption coincides with the basic tenet of the so-called color-singlet model [3–7]. Quarkonium production is presumed in this model to be mediated by parton reactions that generate colorless heavy quark-antiquark pairs with the same quantum numbers as the mesons into which they nonperturbatively evolve. Transverse momentum distributions calculated within this picture badly underestimate experimental observations for  $p_\perp \gtrsim 2M_Q$ . The breakdown of the color-singlet model stems from its neglect of all high energy processes that create  $Q\bar{Q}$  pairs with quantum numbers different from those of the final state meson. In particular, it overlooks short distance contributions to quarkonia cross sections from intermediate color-octet states which can be orders of magnitude larger than those from color-singlet pairs. Even if the long distance hadronization of the former is suppressed by several powers of  $v$  compared to the latter, the color-octet components of quarkonia distributions can dominate overall.

In a previous paper [8], we examined the contributions to hadron collider quarkonia cross sections from processes which create colored heavy quark-antiquark pairs in  $L = 0$ ,  $S = 1$  configurations at short distance scales. Such  $Q\bar{Q}[{}^3S_1^{(8)}]$  pairs may emit or absorb a soft chromoelectric dipole gluon and evolve at  $O(v^5)$  into  $\chi_{QJ}$  mesons. These P-wave quarkonia can later radiatively decay to lower S-wave  $\psi_Q$  levels. Alternatively,  $Q\bar{Q}[{}^3S_1^{(8)}]$  pairs may undergo double chromoelectric dipole transitions and directly hadronize at  $O(v^7)$  into  $\psi_Q$  mesons. The first channel formally represents the dominant color-octet production

mechanism. But since  $\chi_{QJ} \rightarrow \psi_Q + \gamma$  branching ratios in both the charmonia and bottomonia sectors are numerically comparable to  $v_c^2 \simeq 0.23$  and  $v_b^2 \simeq 0.08$ , the second mode is phenomenologically important as well. Consistency then requires that  $O(v^7)$  color-octet contributions to  $\psi_Q$  production from colored  $L = S = 0$  and  $L = S = 1$  states also be considered. Therefore, we calculate in this article the  $\psi_Q$  cross sections arising from  $Q\bar{Q}[{}^1S_0^{(8)}]$  and  $Q\bar{Q}[{}^3P_J^{(8)}]$  intermediate channels. As we shall see, inclusion of a fully consistent set of color-octet quarkonia cross sections brings theoretical predictions into line with experimental observations of prompt Psi and Upsilon production at Fermilab.

Our paper is organized as follows. In section 2, we compute the amplitudes for  $gg \rightarrow Q\bar{Q}[{}^1S_0^{(8)}]$  and  $gg \rightarrow Q\bar{Q}[{}^3P_J^{(8)}]$  scattering which mediate  $\psi_Q$  production at small transverse momenta. We then utilize these amplitudes in section 3 to determine the  $Q\bar{Q}[{}^1S_0^{(8)}]$  and  $Q\bar{Q}[{}^3P_J^{(8)}]$  contributions to  $\psi_Q$  differential cross sections in  $2 \rightarrow 2$  collisions. In section 4, we fit color-octet quarkonia distributions to recent Psi and Upsilon measurements and determine improved numerical values for several NRQCD matrix elements. Finally, we summarize our findings in section 5 and close with some thoughts on the implications of our results for quarkonia production in several different experimental settings.

## 2. $\psi_Q$ production in $2 \rightarrow 1$ collisions

Color-octet quarkonia production starts at  $O(\alpha_s^2)$  with the scattering processes  $q + \bar{q} \rightarrow Q + \bar{Q}$  and  $g + g \rightarrow Q + \bar{Q}$ . The Feynman diagrams which mediate these reactions are illustrated in fig. 1 and fig. 2. In the first quark scattering channel, the heavy quark-antiquark pair appearing in the final state must share the same quantum numbers as its intermediate virtual gluon progenitor. Angular momentum, parity and charge conjugation conservation restrict the spin, orbital and total angular momentum quantum numbers of the  $Q\bar{Q}$  pair to  $L = 0$  or  $2$ ,  $S = 1$  and  $J = 1$ . In the second gluon scattering process, the allowed values for  $L$ ,  $S$  and  $J$  are not so tightly prescribed. In ref. [8], we examined the important special case where gluon fusion produces  $Q\bar{Q}[{}^3S_1^{(8)}]$  pairs. We now generalize our earlier analysis and consider the  $O(\alpha_s^2)$  formation of other pairs with different sets of quantum numbers.

To begin, we write down the on-shell scattering amplitude

$$\begin{aligned} \mathcal{A} \left( g_a(p_1)g_b(p_2) \rightarrow Q^i \left( \frac{P}{2} + q; s_1 \right) \bar{Q}_j \left( \frac{P}{2} - q; s_2 \right) \right) &= -2g_s^2 \varepsilon^\mu(p_1) \varepsilon^\nu(p_2) \\ &\times \bar{u} \left( \frac{P}{2} + q; s_1 \right) \left\{ (T_a T_b)_j^i \frac{\gamma_\mu [\not{p}_2 - \not{p}_1 + 2\not{q} + 2M_Q] \gamma_\nu}{(p_2 - p_1 + 2q)^2 - 4M_Q^2} + (T_b T_a)_j^i \frac{\gamma_\nu [\not{p}_1 - \not{p}_2 + 2\not{q} + 2M_Q] \gamma_\mu}{(p_2 - p_1 - 2q)^2 - 4M_Q^2} \right. \\ &\left. - \frac{i}{8M_Q^2} f_{abc} (T_c)_j^i [g_{\mu\nu} (\not{p}_2 - \not{p}_1) + 2(p_{1\nu} \gamma_\mu - p_{2\mu} \gamma_\nu)] \right\} v \left( \frac{P}{2} - q; s_2 \right) \end{aligned} \quad (2.1)$$

that corresponds to the sum of the three graphs displayed in fig. 2. The reduced amplitude which describes the creation of a  $Q\bar{Q}$  pair in a particular angular momentum and color configuration is obtained from this expression by applying a series of projection operations:

$$\begin{aligned} \mathcal{A} \left( g_a(p_1)g_b(p_2) \rightarrow Q\bar{Q} [^{2S+1}L_J^{(1,8c)}](P) \right) &= \\ \sum_{L_Z, S_Z} \sum_{s_1, s_2} \sum_{i, j} \int \frac{d^3 q}{(2\pi)^3 2q^0} \delta(q^0 - \frac{\vec{q}^2}{M}) Y_{L_Z}^*(\hat{q}) \langle \frac{1}{2} s_1; \frac{1}{2} s_2 | SS_Z \rangle \langle LL_Z; SS_Z | JJ_Z \rangle \langle 3i; \bar{3}j | 1, 8c \rangle \\ &\times \mathcal{A} \left( g_a(p_1)g_b(p_2) \rightarrow Q^i \left( \frac{P}{2} + q; s_1 \right) \bar{Q}_j \left( \frac{P}{2} - q; s_2 \right) \right). \end{aligned} \quad (2.2)$$

Several points about this projection formula should be noted. Firstly, a  $Q\bar{Q}$  pair has negligible overlap with a nonrelativistic quarkonium bound state unless the relative momentum  $q$  between the heavy quark and antiquark is small compared to their combined momentum  $P$ . We have therefore incorporated a delta function into (2.2) which restricts the triple integral over  $q$  to the two-dimensional surface defined by  $|\vec{q}| = \sqrt{Mq^0}$  where  $q^0 \simeq Mv^2 \ll M \equiv 2M_Q$ . The squared invariant mass of the  $Q\bar{Q}$  pair thus equals  $P^2 = M^2$  up to small relativistic corrections. Inclusion of the delta function also properly converts the mass dimension of the  $2 \rightarrow 2$  scattering amplitude into that for a  $2 \rightarrow 1$  reaction. Secondly, the angular integration over the spherical harmonic projects out the pair's specified partial wave. The sums over the Clebsch-Gordan coefficients similarly project out the spin and total angular momentum of the  $Q\bar{Q}$  object. Finally, the sum over the  $SU(3)$  coefficients

$$\begin{aligned} \langle 3i; \bar{3}j | 1 \rangle &= \delta_i^j / \sqrt{N_c} \\ \langle 3i; \bar{3}j | 8c \rangle &= \sqrt{2} (T_c)_i^j \end{aligned} \quad (2.3)$$

combines together the color quantum numbers of the quark and antiquark into either a singlet or octet configuration.

Inserting the gluon scattering amplitude (2.1) into the projection formula in (2.2), we can readily calculate the reduced amplitude for two gluons to fuse into an arbitrary color-octet combination. We list below the formation amplitudes for  $Q\bar{Q}[{}^3S_1^{(8)}]$ ,  $Q\bar{Q}[{}^1S_0^{(8)}]$  and  $Q\bar{Q}[{}^3P_J^{(8)}]$  pairs which all hadronize into  $\psi_Q$  bound states at  $O(v^7)$  in the velocity expansion:

$$\begin{aligned} \mathcal{A}(g_a(p_1)g_b(p_2) \rightarrow Q\bar{Q}[{}^3S_1^{(8)}]_c) &= \frac{i}{4(2\pi)^3} \sqrt{\frac{4\pi M}{q^0}} g_s^2 f_{abc} \varepsilon^\mu(p_1) \varepsilon^\nu(p_2) \varepsilon^\sigma(S_z)^* \\ &\times \frac{p_1^2 + p_2^2}{p_1^2 + p_2^2 - M^2} [(p_2 - p_1)_\sigma g_{\mu\nu} + 2(p_{1\nu} g_{\mu\sigma} - p_{2\mu} g_{\nu\sigma})] \end{aligned} \quad (2.4a)$$

$$\mathcal{A}(g_a(p_1)g_b(p_2) \rightarrow Q\bar{Q}[{}^1S_0^{(8)}]_c) = -\frac{i}{2(2\pi)^3} \sqrt{\frac{4\pi M}{q^0}} g_s^2 d_{abc} \frac{M \epsilon_{\sigma\tau\mu\nu} p_1^\sigma p_2^\tau \varepsilon^\mu(p_1) \varepsilon^\nu(p_2)}{p_1^2 + p_2^2 - M^2} \quad (2.4b)$$

$$\begin{aligned} \mathcal{A}(g_a(p_1)g_b(p_2) \rightarrow Q\bar{Q}[{}^3P_J^{(8)}]_c) &= \frac{1}{2(2\pi)^3} \sqrt{\frac{4\pi}{3}} g_s^2 d_{abc} \sum_{L_Z, S_Z} \langle 1L_Z; 1S_Z | J J_Z \rangle \varepsilon^\alpha(L_Z)^* \varepsilon^\beta(S_Z)^* \\ &\times \frac{M \varepsilon^\mu(p_1) \varepsilon^\nu(p_2)}{p_1^2 + p_2^2 - M^2} \left\{ g_{\alpha\mu} p_{1\nu} (p_2 - p_1)_\beta + g_{\alpha\nu} p_{2\mu} (p_1 - p_2)_\beta \right. \\ &\quad + (p_2^2 - p_1^2 - M^2) g_{\alpha\nu} g_{\beta\mu} + (p_1^2 - p_2^2 - M^2) g_{\alpha\mu} g_{\beta\nu} \\ &\quad + \frac{M^2}{M^2 - p_1^2 - p_2^2} [g_{\mu\nu} p_{1\beta} (p_1 - p_2)_\alpha + g_{\mu\nu} p_{2\beta} (p_2 - p_1)_\alpha] \\ &\quad \left. + \frac{M^2 + p_1^2 + p_2^2}{M^2 - p_1^2 - p_2^2} [g_{\mu\beta} p_{1\nu} (p_2 - p_1)_\alpha + g_{\nu\beta} p_{2\mu} (p_1 - p_2)_\alpha] \right\}. \end{aligned} \quad (2.4c)$$

As required by gauge invariance, these expressions vanish when  $p_1^2 = p_2^2 = 0$  and  $\varepsilon^\mu(p_1) \rightarrow p_1^\mu$  or  $\varepsilon^\nu(p_2) \rightarrow p_2^\nu$ . The general P-wave result listed in (2.4c) may be further reduced by employing the Clebsch-Gordan identities [6]

$$\begin{aligned} \sum_{L_Z, S_Z} \langle 1L_Z; 1S_Z | 00 \rangle \varepsilon^\alpha(L_Z)^* \varepsilon^\beta(S_Z)^* &= \sqrt{\frac{1}{3}} (g^{\alpha\beta} - \frac{P^\alpha P^\beta}{M^2}) \\ \sum_{L_Z, S_Z} \langle 1L_Z; 1S_Z | 1J_Z \rangle \varepsilon^\alpha(L_Z)^* \varepsilon^\beta(S_Z)^* &= -\frac{i}{\sqrt{2}M} \epsilon^{\alpha\beta\gamma\delta} P_\gamma \varepsilon_\delta(J_Z)^* \\ \sum_{L_Z, S_Z} \langle 1L_Z; 1S_Z | 2J_Z \rangle \varepsilon^\alpha(L_Z)^* \varepsilon^\beta(S_Z)^* &= \varepsilon^{\alpha\beta}(J_Z)^*. \end{aligned} \quad (2.5)$$

We then find that  $gg \rightarrow Q\bar{Q}[{}^3P_1^{(8)}]$  as well as  $gg \rightarrow Q\bar{Q}[{}^3S_1^{(8)}]$  scattering vanishes when both incident gluons go on-shell [8,9].

The projection formula in (2.2) can obviously be generalized to other parton channels besides  $gg \rightarrow Q\bar{Q}[{}^{2S+1}L_J^{(1,8)}]$ . We may insert any QCD amplitude which has a heavy

quark and antiquark appearing in the final state and project out a reduced color-singlet or color-octet expression. Applying this general technique to the  $q\bar{q} \rightarrow Q\bar{Q}$  scattering process pictured in fig. 1, we find

$$\mathcal{A}(q(p_1)\bar{q}(p_2) \rightarrow Q\bar{Q}[{}^3S_1^{(8)}]_a) = \frac{1}{4(2\pi)^3} \sqrt{\frac{4\pi M}{q^0}} g_s^2 \bar{v}(p_2) \gamma_\sigma T_a u(p_1) \varepsilon^\sigma(S_z)^*. \quad (2.6)$$

In ref. [8], we performed a less general projection operation which did not explicitly involve a relative momentum integration nor a partial wave decomposition of  $\mathcal{A}(q\bar{q} \rightarrow Q\bar{Q})$ . The corresponding reduced amplitude listed in eqn. (2.10) of ref. [8] thus differs from the result displayed above by an overall multiplicative factor.

The squares of  $2 \rightarrow 1$  amplitudes enter into the differential cross section for heavy pair production

$$d\sigma \left( a(p_1)b(p_2) \rightarrow Q\bar{Q}[{}^{2S+1}L_J^{(1,8)}](P) \right) = \frac{1}{4p_1 p_2} \overline{\sum} \left| \mathcal{A}(ab \rightarrow Q\bar{Q}[{}^{2S+1}L_J^{(1,8)}]) \right|^2 d\Phi_1(p_1+p_2; P) \quad (2.7)$$

where the barred summation symbol indicates that initial (final) spins and colors are averaged (summed) and  $d\Phi_1$  denotes a one-body phase space factor. High and low energy effects are intertwined in this expression. In order to disentangle it, we follow ref. [1] and match the integrated cross section onto the product of a short distance coefficient and a long distance NRQCD matrix element:

$$\sigma \left( ab \rightarrow Q\bar{Q}[{}^{2S+1}L_J^{(1,8)}] \right) = \frac{C_{\text{short}}}{M_Q^{d-4}} \times \langle 0 | \mathcal{O}_{1,8}^{Q\bar{Q}}({}^{2S+1}L_J) | 0 \rangle. \quad (2.8)$$

The general structure of the operator whose vacuum-to-vacuum matrix element appears on the RHS of this matching condition looks like

$$\mathcal{O}_{1,8}^{Q\bar{Q}}({}^{2S+1}L_J) = \chi^\dagger K \psi \left( \sum_{m_J} \left| Q\bar{Q}[{}^{2S+1}L_J^{(1,8)}] \right\rangle \left\langle Q\bar{Q}[{}^{2S+1}L_J^{(1,8)}] \right| \right) \psi^\dagger K \chi \quad (2.9)$$

where  $\psi$  and  $\chi$  represent two-component Pauli spinor fields and the matrix  $K$  denotes a product of color, spin and covariant derivative factors. The intermediate quark-antiquark state sandwiched in the middle

$$\begin{aligned} \left| Q\bar{Q}[{}^{2S+1}L_J^{(1,8)}] \right\rangle &= \sum_{L_Z, S_Z} \sum_{s_1, s_2} \sum_{i,j} \int \frac{d^3 q}{(2\pi)^3 2q^0} \delta(q^0 - \frac{\vec{q}^2}{M}) \\ &\times Y_{LL_Z}^*(\hat{q}) \left\langle \frac{1}{2} s_1; \frac{1}{2} s_2 | SS_Z \right\rangle \langle LL_Z; SS_Z | JJ_Z \rangle \langle 3i; \bar{3}j | 1, 8 \rangle \left| Q^i(q; s_1) \bar{Q}_j(-q; s_2) \right\rangle \end{aligned} \quad (2.10)$$

is defined in the NRQCD effective theory in the same way as in full QCD. As a result, any arbitrariness in the definitions of the heavy pair production cross section and NRQCD matrix element cancels out of their ratio. The short distance coefficient appearing on the RHS of (2.8) is convention independent.

All information related to the hard scattering process which creates the  $Q\bar{Q}$  pair is encoded within  $C_{\text{short}}$ . This same coefficient enters into the physical quarkonium production cross section

$$\sigma \left( ab \rightarrow Q\bar{Q}[^{2S+1}L_J^{(1,8)}] \rightarrow \psi_Q + X \right) = \frac{C_{\text{short}}}{M_Q^{(d+1)-4}} \times \langle 0 | \mathcal{O}_{1,8}^{\psi_Q}(^{2S+1}L_J) | 0 \rangle. \quad (2.11)$$

On the other hand, the accompanying long distance matrix element which specifies the probability that a  $Q\bar{Q}[^{2S+1}L_J^{(1,8)}]$  pair hadronizes into a  $\psi_Q$  bound state is completely different from its counterpart in (2.8). The operator

$$\mathcal{O}_{1,8}^{\psi_Q}(^{2S+1}L_J) = \chi^\dagger K \psi \left( \sum_{m_J} \sum_X |\psi_Q + X\rangle \langle \psi_Q + X| \right) \psi^\dagger K \chi \quad (2.12)$$

has one unit greater mass dimension than  $\mathcal{O}_{1,8}^{Q\bar{Q}}(^{2S+1}L_J)$  as can be verified by comparing the dimensions of heavy intermediate pair and nonrelativistically normalized  $\psi_Q$  states. The inverse powers of  $M_Q$  in cross section equations (2.8) and (2.11) consequently differ by unity. The nonperturbative matrix element  $\langle 0 | \mathcal{O}_{1,8}^{\psi_Q}(^{2S+1}L_J) | 0 \rangle$  also cannot readily be calculated within NRQCD unlike its perturbative  $\langle 0 | \mathcal{O}_{1,8}^{Q\bar{Q}}(^{2S+1}L_J) | 0 \rangle$  counterpart. Simple multiplicity relations such as

$$\begin{aligned} \langle 0 | \mathcal{O}_{1,8}^H(^3S_1) | 0 \rangle &= 3 \langle 0 | \mathcal{O}_{1,8}^H(^1S_0) | 0 \rangle \\ \langle 0 | \mathcal{O}_{1,8}^H(^3P_J) | 0 \rangle &= (2J+1) \langle 0 | \mathcal{O}_{1,8}^H(^3P_0) | 0 \rangle \end{aligned} \quad (2.13)$$

are obeyed exactly by the latter and approximately by the former. But the color-factor relation

$$\langle 0 | \mathcal{O}_8^H(^{2S+1}L_J) | 0 \rangle = \frac{N_c^2 - 1}{2N_c} \langle 0 | \mathcal{O}_1^H(^{2S+1}L_J) | 0 \rangle \quad (2.14)$$

which holds for  $H = Q\bar{Q}$  certainly does not apply when  $H = \psi_Q$ . Numerical values for  $\langle 0 | \mathcal{O}_{1,8}^{\psi_Q}(^{2S+1}L_J) | 0 \rangle$  matrix elements must be extracted either from experimental data or lattice calculations.

In order to clarify the meaning of these NRQCD matching ideas, we explicitly evaluate the matching conditions specified in eqns. (2.8) and (2.11) for one simple example. We

consider the gluon fusion formation of an  $\eta_Q$  pseudoscalar meson through an intermediate  $Q\bar{Q}[{}^1S_0^{(1)}]$  pair. A straightforward computation yields the color-singlet cross section

$$\sigma \left( gg \rightarrow Q\bar{Q}[{}^1S_0^{(1)}] \right) = \frac{\alpha_s^2}{384\pi^2} \frac{M}{q^0 \hat{s}} \delta \left( 1 - \frac{M^2}{\hat{s}} \right) \quad (2.15)$$

and matrix element

$$\langle 0 | \mathcal{O}_1^{Q\bar{Q}}({}^1S_0) | 0 \rangle = \left\langle 0 \left| \chi^\dagger \psi \right| Q\bar{Q}[{}^1S_0^{(1)}] \right\rangle \left\langle Q\bar{Q}[{}^1S_0^{(1)}] \left| \psi^\dagger \chi \right| 0 \right\rangle = \frac{N_c}{128\pi^5} \frac{M^3}{q^0}. \quad (2.16)$$

We derived this last result within the NRQCD effective theory by decomposing the Pauli fields

$$\begin{aligned} \psi_\alpha^i(x) &= \sum_{s=1}^2 \int \frac{d^3 p}{(2\pi)^3} b^i(p; s) \xi_\alpha(p, s) e^{-ip \cdot x} \\ \chi_{i\alpha}(x) &= \sum_{s=1}^2 \int \frac{d^3 p}{(2\pi)^3} c_i^\dagger(p; s) \eta_\alpha(p, s) e^{ip \cdot x} \end{aligned} \quad (2.17)$$

in terms of two-component spinors normalized according to

$$\sum_{s=1}^2 \xi_\alpha(p, s) \xi_\beta^\dagger(p, s) = \sum_{s=1}^2 \eta_\alpha(p, s) \eta_\beta^\dagger(p, s) = \delta_{\alpha\beta} \quad (2.18)$$

and single fermion creation and annihilation operators which satisfy the nonrelativistic anticommutation relations

$$\{b^i(p; s), b_j^\dagger(p'; s')\} = \{c^i(p; s), c_j^\dagger(p'; s')\} = (2\pi)^3 \delta_j^i \delta_{ss'} \delta^{(3)}(p - p'). \quad (2.19)$$

Taking the ratio of (2.15) and (2.16), we deduce the short distance coefficient in matching condition (2.8)

$$\frac{C(gg \rightarrow Q\bar{Q}[{}^1S_0^{(1)}])_{\text{short}}}{M_Q^{d-4}} = \frac{1}{9} \frac{\pi^3 \alpha_s^2}{M^2 \hat{s}} \delta \left( 1 - \frac{M^2}{\hat{s}} \right) \quad (2.20)$$

and the gluon fusion cross section in matching condition (2.11):

$$\sigma \left( gg \rightarrow Q\bar{Q}[{}^1S_0^{(1)}] \rightarrow \eta_Q \right) = \frac{2}{9} \frac{\pi^3 \alpha_s^2}{M^3 \hat{s}} \delta \left( 1 - \frac{M^2}{\hat{s}} \right) \langle 0 | \mathcal{O}_1^{\eta_Q}({}^1S_0) | 0 \rangle. \quad (2.21)$$

If we recall the relation between the NRQCD matrix element and squared  $\eta_Q$  wavefunction at the origin [1]

$$\langle 0 | \mathcal{O}_1^{\eta_Q}({}^1S_0) | 0 \rangle = \frac{N_c}{2\pi} R(0)^2 (1 + O(v^4)), \quad (2.22)$$

we see that our result is consistent with the  $O(\alpha_s^2)$  cross section

$$\sigma \left( gg \rightarrow Q\bar{Q}[{}^1S_0^{(1)}] \rightarrow \eta_Q \right) = \frac{1}{3} \frac{\pi^2 \alpha_s^2}{M^3 \hat{s}} \delta \left( 1 - \frac{M^2}{\hat{s}} \right) R(0)^2 \quad (2.23)$$

previously reported in the literature [7].

Working in a similar fashion, we can decompose any color-singlet or color-octet cross section into products of short and long distance factors. We tabulate in the Appendix all  $O(\alpha_s^2)$  short distance squared amplitudes for  $2 \rightarrow 1$  color-octet reactions which yield  $\psi_Q$  bound states at  $O(v^7)$  in the NRQCD velocity expansion. The corresponding long distance factors are simply given by appropriate NRQCD matrix elements for specific production channels. For example, the total squared amplitude for  $gg \rightarrow Q\bar{Q}[{}^1S_0^{(8)}] \rightarrow \psi_Q$  scattering equals the product of the process-independent high energy expression listed in eqn. (A.2a) and the process-specific low energy matrix element  $\langle 0 | O_8^{\psi_Q}({}^1S_0) | 0 \rangle$ :

$$\sum \left| \mathcal{A}(gg \rightarrow Q\bar{Q}[{}^1S_0^{(8)}] \rightarrow \psi_Q) \right|^2 = \frac{5(4\pi\alpha_s)^2}{192M} \langle 0 | O_8^{\psi_Q}({}^1S_0) | 0 \rangle. \quad (2.24)$$

Color-octet pair production in  $2 \rightarrow 1$  collisions could represent an important source of quarkonia in fixed target experiments, and its impact needs to be studied. But before definite predictions can be made, numerical values for color-octet matrix elements must be known. Therefore, we now turn to consider quarkonia production at hadron colliders where we can use experimental data to determine these matrix element values.

### 3. $\psi_Q$ production in $2 \rightarrow 2$ collisions

In order to be experimentally detectable, quarkonia must be created at collider facilities with nonvanishing transverse momenta so that they are not lost down the beampipe. Hadrons resulting from  $2 \rightarrow 1$  scattering processes typically have small  $p_\perp$  comparable to the QCD scale. The production of quarkonia with nonnegligible transverse momenta therefore mainly proceeds through  $2 \rightarrow 2$  collisions. Such reactions start at  $O(\alpha_s^3)$  via the parton channels  $q\bar{q} \rightarrow Q\bar{Q}[{}^{2S+1}L_J^{(1,8)}]g$ ,  $gq \rightarrow Q\bar{Q}[{}^{2S+1}L_J^{(1,8)}]q$  and  $gg \rightarrow Q\bar{Q}[{}^{2S+1}L_J^{(1,8)}]g$ . In ref. [8], we calculated the differential production cross sections for  $L = 0, S = 1$  color-octet pairs. In this section, we generalize our previous results and consider the formation of colored  $L = S = 0$  and  $L = S = 1$  pairs.

The Feynman diagrams which mediate quarkonia production in these color-octet channels are illustrated in fig. 3. The shaded circles appearing in the figure represent the

$gg \rightarrow Q\bar{Q}[{}^1S_0^{(8)}]$  and  $gg \rightarrow Q\bar{Q}[{}^3P_J^{(8)}]$  amplitudes in eqns. (2.4b) and (2.4c). The  $q\bar{q} \rightarrow \psi_Q g$  and  $gq \rightarrow \psi_Q q$  diagrams pictured in figs. 3a and 3b can readily be squared using standard spinor summation techniques. On the other hand, conventional evaluation of the gluon channel graphs in fig. 3c represents a formidable computational task. It is therefore advisable to find a more tractable method for calculating the color-octet contributions to  $gg \rightarrow \psi_Q g$  scattering.

We adopt a simple helicity amplitude technique to sum and square the gluon graphs in fig. 3c. We first choose the following explicit representations for the gluon momenta and polarization vectors shown in the figure:

$$\begin{aligned} p_1 &= \frac{\sqrt{\hat{s}}}{2}(1, 0, 0, 1) & \varepsilon_1^+ = \varepsilon_2^- = -\frac{1}{\sqrt{2}}(0, 1, i, 0) \\ p_2 &= \frac{\sqrt{\hat{s}}}{2}(1, 0, 0, -1) & \varepsilon_1^- = \varepsilon_2^+ = \frac{1}{\sqrt{2}}(0, 1, -i, 0) \\ p_4 &= \frac{\hat{s} - M^2}{2\sqrt{\hat{s}}}(1, 0, \sin\theta, -\cos\theta) & (\varepsilon_4^\pm)^* = \frac{1}{\sqrt{2}}(0, \pm 1, i \cos\theta, i \sin\theta). \end{aligned} \quad (3.1)$$

We next boost the the heavy pair's four-momentum from its primed rest frame to the unprimed lab frame:

$$p'_3 = (M, 0, 0, 0) \rightarrow p_3 = \left( \frac{\hat{s} + M^2}{2\sqrt{\hat{s}}}, 0, -\frac{\hat{s} - M^2}{2\sqrt{\hat{s}}} \sin\theta, \frac{\hat{s} - M^2}{2\sqrt{\hat{s}}} \cos\theta \right). \quad (3.2)$$

We also Lorentz transform the rest frame polarization vectors and tensors

$$\begin{aligned} (\varepsilon'_3{}^{(h=1)})^* &= -\sqrt{\frac{1}{2}} \begin{pmatrix} 0 \\ 1 \\ -i \\ 0 \end{pmatrix} & (\varepsilon'_3{}^{(h=0)})^* &= \sqrt{\frac{2}{3}} \begin{pmatrix} 0 & 0 & 0 & 0 \\ 0 & -\frac{1}{2} & 0 & 0 \\ 0 & 0 & -\frac{1}{2} & 0 \\ 0 & 0 & 0 & 1 \end{pmatrix} \\ (\varepsilon'_3{}^{(h=0)})^* &= \begin{pmatrix} 0 \\ 0 \\ 0 \\ 1 \end{pmatrix} & (\varepsilon'_3{}^{(h=\pm 1)})^* &= \mp \frac{1}{2} \begin{pmatrix} 0 & 0 & 0 & 0 \\ 0 & 0 & 0 & 1 \\ 0 & 0 & 0 & \mp i \\ 0 & 1 & \mp i & 0 \end{pmatrix} \\ (\varepsilon'_3{}^{(h=-1)})^* &= \sqrt{\frac{1}{2}} \begin{pmatrix} 0 \\ 1 \\ i \\ 0 \end{pmatrix} & (\varepsilon'_3{}^{(h=\pm 2)})^* &= \frac{1}{2} \begin{pmatrix} 0 & 0 & 0 & 0 \\ 0 & 1 & \mp i & 0 \\ 0 & \mp i & -1 & 0 \\ 0 & 0 & 0 & 0 \end{pmatrix} \end{aligned} \quad (3.3)$$

of  $J = 1$  and  $J = 2$   $Q\bar{Q}$  pairs. Given these explicit representations, it is easy to work out all possible scalar contractions and express the answers in terms of the Mandelstam

invariants  $\hat{s}$ ,  $\hat{t} = -(\hat{s} - M^2)(1 - \cos \theta)/2$  and  $\hat{u} = -(\hat{s} - M^2)(1 + \cos \theta)/2$ . The gluon channel amplitudes are functions of these Lorentz invariant dot products.

Using the high energy physics package FEYNCALC [14], we calculated each individual helicity amplitude for  $gg \rightarrow Q\bar{Q}[1S_0^{(8)}]g$  and  $gg \rightarrow Q\bar{Q}[3P_J^{(8)}]g$  scattering. Parity and crossing symmetry relations between different helicity amplitudes provided valuable checks on our Mathematica code. Since separate helicity amplitudes do not interfere, the total squared amplitude simply equals the sum of the squared helicity amplitudes. The final results for the  $gg \rightarrow Q\bar{Q}[2S+1L_J^{(8)}]g$  channel are displayed in the Appendix alongside those for the  $q\bar{q} \rightarrow Q\bar{Q}[2S+1L_J^{(8)}]g$  and  $gq \rightarrow Q\bar{Q}[2S+1L_J^{(8)}]q$  modes. For completeness, we include in this list the  $Q\bar{Q}[3S_1^{(8)}]$  squared amplitudes which we calculated in ref. [8].

The products of short distance color-octet squared amplitudes and long distance NRQCD matrix elements enter into the partonic cross section

$$\begin{aligned} \frac{d\sigma}{d\hat{t}}(ab \rightarrow Q\bar{Q}[2S+1L_J^{(8)}]c \rightarrow \psi_Q)_{\text{octet}} = \\ \frac{1}{16\pi\hat{s}^2} \overline{\sum} \left| \mathcal{A}(ab \rightarrow Q\bar{Q}[2S+1L_J^{(8)}]c)_{\text{short}} \right|^2 \langle 0 | O_8^{\psi_Q}(2S+1L_J) | 0 \rangle. \end{aligned} \quad (3.4)$$

After folding in distribution functions  $f_{a/A}(x_a)$  and  $f_{b/B}(x_b)$  that specify the probabilities of finding partons  $a$  and  $b$  inside hadrons  $A$  and  $B$  carrying momentum fractions  $x_a$  and  $x_b$ , we obtain the hadronic cross section

$$\frac{d^3\sigma}{dy_3 dy_4 dp_\perp} (AB \rightarrow \psi_Q X)_{\text{octet}} = 2p_\perp \sum_{abc} x_a x_b f_{a/A}(x_a) f_{b/B}(x_b) \frac{d\sigma}{d\hat{t}}(ab \rightarrow Q\bar{Q}[2S+1L_J^{(8)}]c \rightarrow \psi_Q)_{\text{octet}} \quad (3.5)$$

which is a function of the  $\psi_Q$  and recoiling jet rapidities  $y_3$  and  $y_4$  and their common transverse momentum  $p_\perp$ . With this hadronic distribution in hand, we can determine color-octet contributions to  $\psi_Q$  production in any hadronic process. We apply it to the study of charmonia and bottomonia at Fermilab in the following section.

#### 4. Psi and Upsilon production at the Tevatron

During the past few years, striking disparities have arisen between old predictions and new measurements of  $J/\psi$ ,  $\psi'$  and  $\Upsilon$  production at the Tevatron. The CDF collaboration has detected these heavy mesons at rates which exceed theoretical expectations based upon the color-singlet model by orders of magnitude [10–12]. In ref. [8], we examined the impact of  $c\bar{c}[3S_1^{(8)}]$  and  $b\bar{b}[3S_1^{(8)}]$  intermediate states upon Psi and Upsilon production. Since

numerical values for most NRQCD color-octet matrix elements were unknown, we simply fitted the magnitudes of  $d\sigma/dp_\perp(p\bar{p} \rightarrow \psi_Q + X)_{\text{octet}}$  cross sections to the CDF data. We found that including the  $Q\bar{Q}[{}^3S_1^{(8)}]$  channel significantly diminished discrepancies between the shapes of the predicted and measured transverse momentum distributions. We now update our earlier analysis and incorporate cross section contributions from  $Q\bar{Q}[{}^1S_0^{(8)}]$  and  $Q\bar{Q}[{}^3P_J^{(8)}]$  pairs. As we shall see, the fully consistent  $O(v^7)$  set of color-octet differential cross sections yields substantially improved fits to the data.

We first plot in fig. 4 the ratio

$$R(p_\perp) = \frac{\sum_{J=0}^2 \frac{d\sigma}{dp_\perp} (p\bar{p} \rightarrow Q\bar{Q}[{}^3P_J^{(8)}] + X \rightarrow \psi_Q + X)}{\frac{d\sigma}{dp_\perp} (p\bar{p} \rightarrow Q\bar{Q}[{}^1S_0^{(8)}] + X \rightarrow \psi_Q + X)} \quad (4.1)$$

where we temporarily set  $\langle \mathcal{O}_8^{\psi_Q}({}^3P_0) \rangle = M_Q^2 \langle \mathcal{O}_8^{\psi_Q}({}^1S_0) \rangle$  for comparison purposes.<sup>1</sup> The solid curve's nearly constant value  $R(p_\perp) \simeq 3$  for  $p_\perp \gtrsim 5$  GeV indicates that the shapes of the  $c\bar{c}[{}^1S_0^{(8)}]$  and  $c\bar{c}[{}^3P_J^{(8)}]$  differential cross sections are practically identical in the charmonia sector. As a result, all fits for the NRQCD matrix elements in these color-octet channels become degenerate when performed over the transverse momentum range  $5 \text{ GeV} \leq p_\perp \leq 20 \text{ GeV}$  where  $J/\psi$  and  $\psi'$  differential cross sections have been measured. We consequently can only extract the linear combination  $\langle \mathcal{O}_8^{\psi}({}^3P_0) \rangle / M_c^2 + \langle \mathcal{O}_8^{\psi}({}^1S_0) \rangle / 3$  along with  $\langle \mathcal{O}_8^{\psi}({}^3S_1) \rangle$  from the CDF data. In the bottomonia sector, the shapes of the  $b\bar{b}[{}^1S_0^{(8)}]$  and  $b\bar{b}[{}^3P_J^{(8)}]$  distributions are not exactly the same throughout the  $0 \leq p_\perp \leq 15$  GeV interval where Upsilon data exists. As indicated by the dot-dashed curve in fig. 4,  $R(p_\perp)$  varies around 5 over this transverse momentum range. Yet the differences in shape between the  $b\bar{b}[{}^3P_J^{(8)}]$  and  $b\bar{b}[{}^1S_0^{(8)}]$  contributions to the total Upsilon differential cross section are not sufficiently great so that a full three-parameter color-octet matrix element fit can be reliably performed. So we will simply determine estimates for the linear combination  $\langle \mathcal{O}_8^{\Upsilon}({}^3P_0) \rangle / M_b^2 + \langle \mathcal{O}_8^{\Upsilon}({}^1S_0) \rangle / 5$  along with  $\langle \mathcal{O}_8^{\Upsilon}({}^3S_1) \rangle$ .

Our new fits to prompt charmonia production at the Tevatron within the pseudorapidity interval  $|\eta| \leq 0.6$  are illustrated in fig. 5 and fig. 6. All contributions from  $B$  meson decay have been removed from the data sets displayed in these figures, and radiative  $\chi_{cJ}$

---

<sup>1</sup> The differential cross sections which enter into results displayed in fig. 4 and all subsequent figures were calculated using the MRSD0 parton distribution functions evaluated at the renormalization scale  $\mu = \sqrt{p_\perp^2 + M^2}$ .

decay feeddown to the  $J/\psi$  differential cross section has been separated out as well. The dashed curves depict the direct color-singlet production predictions based upon the charm quark mass value  $M_c = 1.48$  GeV and the Buchmüller-Tye charmonium wave functions at the origin tabulated in ref. [13]. The dot-dashed and dotted curves illustrate the best fits for the  $c\bar{c}[^3S_1^{(8)}]$  and combined  $c\bar{c}[^3P_J^{(8)}]$  plus  $c\bar{c}[^1S_0^{(8)}]$  channels. The solid curves show the sums of the color-singlet and color-octet components and represent the total predicted differential cross sections.

Following the interpolation procedure described in ref. [8], we have included leading log corrections into the  $c\bar{c}[^3S_1^{(8)}]$  differential cross sections so that they approach Altarelli-Parisi improved gluon fragmentation distributions for  $p_\perp \gg M_c$ . In the large transverse momentum limit, gluon fragmentation represents the dominant source of prompt charmonia [15–20]. This asymptotic behavior can be seen in the dotdashed  $c\bar{c}[^3S_1^{(8)}]$  curves of figs. 5 and 6. But throughout the  $0 \leq p_\perp \leq 20$  GeV region, they are not overwhelmingly larger than the combined  $c\bar{c}[^3P_J^{(8)}]$  and  $c\bar{c}[^1S_0^{(8)}]$  components whose contributions to prompt charmonia production are sizable. Inclusion of the latter color-octet channels into the total differential cross sections yields theoretical  $\psi'$  and  $J/\psi$  distributions which fit the data quite well. Their respective  $\chi^2/\text{NDOF} = 0.5$  and  $\chi^2/\text{NDOF} = 0.9$  figures-of-merit are nice and small.

In fig. 7, we plot the transverse momentum distribution of  $J/\psi$  mesons which result from radiative  $\chi_{cJ}$  decay. The dashed curve in the figure shows the color-singlet  $\chi_{cJ}$  differential cross section multiplied by  $\text{Br}(\chi_{cJ} \rightarrow J/\psi + \gamma)$  and summed over  $J = 0, 1$  and  $2$ . The dot-dashed curve illustrates the  $c\bar{c}[^3S_1^{(8)}]$  channel contribution. The solid curve corresponds to their sum and represents the total  $O(v^5)$  cross section prediction. As indicated by its poor  $\chi^2/\text{NDOF} = 2.3$  value, this solid line does not fit the data well. We believe that a better match could be achieved if subleading color-octet contributions were included. The first subdominant corrections enter at  $O(v^9)$  in the NRQCD velocity expansion from the long distance evolution of  $Q\bar{Q}[^3P_J^{(8)}]$ ,  $Q\bar{Q}[^3D_J^{(8)}]$  and  $Q\bar{Q}[^1P_1^{(8)}]$  pairs into  $\chi_{QJ}$  bound states. Since short distance production cross sections for the latter two pairs have not yet been calculated, we cannot legitimately include into fig. 7 subleading contributions from the first pair which we have computed.

We turn now to the bottomonium sector and consider Upsilon production at the Tevatron within the rapidity interval  $|y| \leq 0.4$ . Our new fits to CDF  $\Upsilon(1S)$  and  $\Upsilon(2S)$  data are displayed in fig. 8 and fig. 9. No separation between prompt and delayed Upsilon sources has been experimentally performed. The dashed curves in the figures therefore

include both direct  $\Upsilon$  production and radiative feeddown from  $\chi_{bJ}$  states. These color-singlet distributions are based upon the bottom quark mass value  $M_b = 4.88$  GeV and the Buchmüller-Tye bottomonia wavefunctions at the origin tabulated in ref [13]. The dot-dashed and dotted curves illustrate the  $b\bar{b}[{}^3S_1^{(8)}]$  and combined  $b\bar{b}[{}^3P_J^{(8)}]$  plus  $b\bar{b}[{}^1S_0^{(8)}]$  fits. The solid curves equal the sums of the color-singlet and color-octet contributions and represent the total  $\Upsilon$  differential cross sections. As we previously discussed in ref. [8], the color-singlet and color-octet distributions are corrupted at very small transverse momenta by collinear divergences which should be factored into incident parton distribution functions. Soft gluon effects also need to be resummed before the cross section turnover which is evident in fig. 8 can be properly described. Since we have not incorporated these effects, our cross section predictions are not trustworthy at low  $p_\perp$ . We therefore exclude points in fig. 8 and fig. 9 with  $p_\perp \leq 3.5$  GeV from our fits. We then find  $\chi^2/\text{NDOF} = 0.3$  and  $\chi^2/\text{NDOF} = 0.9$  for the remaining points in these figures.

NRQCD power counting rules provide useful consistency checks on all our fits. We list in tables I and II the numerical values for color-octet matrix elements which we extracted

Color-Octet Matrix Element	Numerical Value (GeV <sup>3</sup> )	NRQCD Scaling Order
$\langle 0   O_8^{J/\psi}({}^3S_1)   0 \rangle$	$(6.6 \pm 2.1) \times 10^{-3}$	$M_c^3 v_c^7$
$\langle 0   O_8^{\chi_{c1}}({}^3S_1)   0 \rangle$	$(9.8 \pm 1.3) \times 10^{-3}$	$M_c^3 v_c^5$
$\langle 0   O_8^{\psi'}({}^3S_1)   0 \rangle$	$(4.6 \pm 1.0) \times 10^{-3}$	$M_c^3 v_c^7$
$\langle 0   O_8^{\Upsilon(1S)}({}^3S_1)   0 \rangle$	$(5.9 \pm 1.9) \times 10^{-3}$	$M_b^3 v_b^7$
$\langle 0   O_8^{\chi_{b1}(1P)}({}^3S_1)   0 \rangle$	$(4.2 \pm 1.3) \times 10^{-1}$	$M_b^3 v_b^5$
$\langle 0   O_8^{\Upsilon(2S)}({}^3S_1)   0 \rangle$	$(4.1 \pm 0.9) \times 10^{-3}$	$M_b^3 v_b^7$
$\langle 0   O_8^{\chi_{b1}(2P)}({}^3S_1)   0 \rangle$	$(3.2 \pm 1.9) \times 10^{-1}$	$M_b^3 v_b^5$

Table I. Color-octet matrix elements

Color-Octet Matrix Element Linear Combination	Numerical Value (GeV <sup>3</sup> )	NRQCD Scaling Order
$\frac{\langle 0 O_8^{J/\psi}(^3P_0) 0\rangle}{M_c^2} + \frac{\langle 0 O_8^{J/\psi}(^1S_0) 0\rangle}{3}$	$(2.2 \pm 0.5) \times 10^{-2}$	$M_c^3 v_c^7$
$\frac{\langle 0 O_8^{\psi'}(^3P_0) 0\rangle}{M_c^2} + \frac{\langle 0 O_8^{\psi'}(^1S_0) 0\rangle}{3}$	$(5.9 \pm 1.9) \times 10^{-3}$	$M_c^3 v_c^7$
$\frac{\langle 0 O_8^{\Upsilon(1S)}(^3P_0) 0\rangle}{M_b^2} + \frac{\langle 0 O_8^{\Upsilon(1S)}(^1S_0) 0\rangle}{5}$	$(7.9 \pm 10.0) \times 10^{-3}$	$M_b^3 v_b^7$
$\frac{\langle 0 O_8^{\Upsilon(2S)}(^3P_0) 0\rangle}{M_b^2} + \frac{\langle 0 O_8^{\Upsilon(2S)}(^1S_0) 0\rangle}{5}$	$(9.1 \pm 7.2) \times 10^{-3}$	$M_b^3 v_b^7$

Table II. Color-octet matrix element linear combinations

from the data along with their scaling dependence upon the heavy quark mass  $M_Q$  and velocity  $v_Q$ . The values for all the charmonia matrix elements were derived directly from the CDF  $J/\psi$  and  $\psi'$  data. On the other hand, insufficient experimental information exists to independently extract  $\langle 0|O_8^{\Upsilon(nS)}(^3S_1)|0\rangle$  and  $\langle 0|O_8^{\chi_{b1}(nP)}(^3S_1)|0\rangle$  in the bottomonia sector. We therefore determined the latter from the Upsilon data after having scaled up the former from the corresponding Psi color-octet matrix elements using NRQCD power counting rules. The remaining  $\langle 0|O_8^{\Upsilon(nS)}(^3P_0)|0\rangle/M_b^2 + \langle 0|O_8^{\Upsilon(nS)}(^1S_0)|0\rangle/5$  linear combinations were obtained directly from the bottomonia cross section data.

The error bars listed in tables I and II are statistical and do not reflect systematic uncertainties in heavy quark masses, color-singlet radial wavefunctions, parton distribution functions and next-to-leading order corrections. The magnitudes of all these different sources of uncertainty can be estimated. For example, the different charm and bottom quark mass values which enter into the power law, logarithmic, Coulomb plus linear and QCD motivated Buchmüller-Tye potentials tabulated in ref. [13] span the ranges  $1.48 \text{ GeV} \leq m_c \leq 1.84 \text{ GeV}$  and  $4.88 \text{ GeV} \leq m_b \leq 5.18 \text{ GeV}$ . These intervals may be

regarded as setting reasonable bounds for the heavy quark mass parameters. The spread in values for radial wavefunctions at the origin calculated in these four different potential models similarly provides an approximate indication of color-singlet matrix element uncertainties. Systematic errors which arise from parton distribution functions and higher order QCD corrections can also be assessed by performing several fits with different choices of distribution functions and renormalization scale. We have not attempted to carry out a detailed analysis of the combined impact of all these systematic uncertainties. Our color-octet matrix element values therefore represent reasonable estimates rather than precise predictions.

Comparing the numbers in table I with their predecessors in table II of ref. [8], we see that the  $Q\bar{Q}[{}^3S_1^{(8)}]$  matrix element values have all diminished. This is not surprising, for some color-octet contributions to quarkonia production are now taken into account by the  $Q\bar{Q}[{}^3P_J^{(8)}]$  and  $Q\bar{Q}[{}^1S_0^{(8)}]$  channels. We also observe that the NRQCD counting rules are more faithfully followed by some matrix elements than others. For instance, the magnitudes of  $\langle \mathcal{O}_8^{J/\psi}({}^3S_1) \rangle$ ,  $\langle \mathcal{O}_8^{\psi'}({}^3S_1) \rangle$  and  $\langle \mathcal{O}_8^{\psi'}({}^3P_0) \rangle/M_c^2 + \langle \mathcal{O}_8^{\psi'}({}^1S_0) \rangle/3$  are all mutually consistent with their common scaling rule. On the other hand,  $\langle \mathcal{O}_8^{\chi_{c1}}({}^3S_1) \rangle$  is somewhat low while  $\langle \mathcal{O}_8^{J/\psi}({}^3P_0) \rangle/M_c^2 + \langle \mathcal{O}_8^{\psi'}({}^1S_0) \rangle/3$  is somewhat high. Since  $v_c^2 \simeq 0.23$  is not very small, none of the charmonia NRQCD order-of-magnitude estimates should be overly interpreted. We view the general consistency of the fitted matrix elements with the power counting rules as an encouraging indication that the color-octet quarkonia production picture is sound.

## 5. Conclusion

In this article, we have calculated the cross sections for producing colored  $L = S = 0$  and  $L = S = 1$  heavy quark-antiquark pairs in hadronic collisions. Intermediate  $Q\bar{Q}[{}^1S_0^{(8)}]$  and  $Q\bar{Q}[{}^3P_J^{(8)}]$  states evolve into  $\psi_Q$  mesons at the same order in the NRQCD velocity expansion as  $Q\bar{Q}[{}^3S_1^{(8)}]$  pairs. Consistency therefore requires that contributions to quarkonia production from all three color-octet channels be considered together. We have found that the full  $O(v^7)$  set of color-octet distributions yields good fits to prompt Psi and Upsilon data collected at the Tevatron. Numerical values for the long distance matrix elements which can be extracted from these data are generally consistent with NRQCD power scaling rules.

Many of the results in this paper can be applied to a range of other interesting problems in quarkonium phenomenology. In particular, the NRQCD matrix elements which

we have extracted from CDF data are universal and hold for color-octet charmonia and bottomonia production at other experimental facilities besides the Tevatron. They can be used, for example, to refine the analysis of the  $J/\psi$  differential cross section measured at the CERN S $\bar{p}$ pS collider which was performed in ref. [21]. It would be interesting to see whether disparities between gluon fragmentation predictions and UA1 data are diminished by including  $Q\bar{Q}[{}^1S_0^{(8)}]$  and  $Q\bar{Q}[{}^3P_J^{(8)}]$  channels [22]. The NRQCD matrix elements can also be applied to the study of quarkonia production at lepton colliders. Gluon fragmentation has been shown to represent the largest source of prompt Psi and Upsilon vector mesons at LEP [23,24]. Its incorporation into  $Z \rightarrow J/\psi$ ,  $Z \rightarrow \psi'$  and  $Z \rightarrow \Upsilon$  branching fractions reduces sizable differences between predictions based upon color-singlet heavy quark fragmentation and recent LEP measurements. Color-octet contributions have similarly been found to play an important role in charmonia production at CLEO [25,26]. Finally, the color-octet mechanism may eliminate disagreements between theory and experiment in fixed target settings.

We look forward to confronting the color-octet production picture with a variety of experimental tests in the near future.<sup>2</sup> It will be interesting to see how well this simple idea can resolve several problems which currently exist in quarkonium physics.

### Acknowledgments

It is a pleasure to thank Michelangelo Mangano, Vaia Papadimitriou, Frank Porter and Mark Wise for helpful discussions.

---

<sup>2</sup> The original preprint version of this article contained a section which discussed predictions for quarkonia spin alignment resulting from the color-octet mechanism. After some errors in our original polarization analysis were pointed out in refs. [27] and [28], we removed this section. We will report our revised spin alignment findings in a future publication.

## Appendix. Color-octet squared amplitudes

We list below short distance squared amplitudes for  $2 \rightarrow 1$  and  $2 \rightarrow 2$  scattering processes which mediate color-octet quarkonia production. These expressions are averaged over initial spins and colors of the two incident partons. The helicity levels of outgoing  $J = 1$  and  $J = 2$  pairs are labeled by the subscript  $h$ . The total squared amplitudes for creating specific quarkonia states are obtained by multiplying these process-independent short distance expressions with appropriate long distance NRQCD matrix elements.

$q\bar{q} \rightarrow Q\bar{Q}[^{2s+1}L_J^{(8)}]$  channel:

$$\overline{\sum_{h=0}} |\mathcal{A}(q\bar{q} \rightarrow Q\bar{Q}[^3S_1^{(8)}])|^2 = 0 \quad (\text{A.1a})$$

$$\overline{\sum_{|h|=1}} |\mathcal{A}(q\bar{q} \rightarrow Q\bar{Q}[^3S_1^{(8)}])|^2 = \frac{(4\pi\alpha_s)^2}{27M} \quad (\text{A.1b})$$

$gg \rightarrow Q\bar{Q}[^{2s+1}L_J^{(8)}]$  channel:

$$\overline{\sum} |\mathcal{A}(gg \rightarrow Q\bar{Q}[^1S_0^{(8)}])|^2 = \frac{5(4\pi\alpha_s)^2}{192M} \quad (\text{A.2a})$$

$$\overline{\sum_{|h|=1}} |\mathcal{A}(gg \rightarrow Q\bar{Q}[^3P_0^{(8)}])|^2 = \frac{5(4\pi\alpha_s)^2}{16M^3} \quad (\text{A.2b})$$

$$\overline{\sum_{h=0}} |\mathcal{A}(gg \rightarrow Q\bar{Q}[^3P_1^{(8)}])|^2 = 0 \quad (\text{A.2c})$$

$$\overline{\sum_{|h|=1}} |\mathcal{A}(gg \rightarrow Q\bar{Q}[^3P_1^{(8)}])|^2 = 0 \quad (\text{A.2d})$$

$$\overline{\sum_{h=0}} |\mathcal{A}(gg \rightarrow Q\bar{Q}[^3P_2^{(8)}])|^2 = 0 \quad (\text{A.2e})$$

$$\overline{\sum_{|h|=1}} |\mathcal{A}(gg \rightarrow Q\bar{Q}[^3P_2^{(8)}])|^2 = 0 \quad (\text{A.2f})$$

$$\overline{\sum_{|h|=2}} |\mathcal{A}(gg \rightarrow Q\bar{Q}[^3P_2^{(8)}])|^2 = \frac{(4\pi\alpha_s)^2}{12M^3} \quad (\text{A.2g})$$

$q\bar{q} \rightarrow Q\bar{Q}[^{2s+1}L_J^{(8)}]g$  channel:

$$\overline{\sum} |\mathcal{A}(q\bar{q} \rightarrow Q\bar{Q}[^1S_0^{(8)}]g)|^2 = \frac{5(4\pi\alpha_s)^3}{27M} \frac{\hat{t}^2 + \hat{u}^2}{\hat{s}(\hat{s} - M^2)^2} \quad (\text{A.3a})$$

$$\overline{\sum_{h=0}} |\mathcal{A}(q\bar{q} \rightarrow Q\bar{Q}[^3S_1^{(8)}]g)|^2 = \frac{8(4\pi\alpha_s)^3}{81M^3} \frac{M^2\hat{s}}{(\hat{s} - M^2)^4} [4(\hat{t}^2 + \hat{u}^2) - \hat{t}\hat{u}] \quad (\text{A.3b})$$

$$\overline{\sum_{|h|=1}} |\mathcal{A}(q\bar{q} \rightarrow Q\bar{Q}[^3S_1^{(8)}]g)|^2 = \frac{2(4\pi\alpha_s)^3}{81M^3} \frac{\hat{s}^2 + M^4}{(\hat{s} - M^2)^4} \frac{\hat{t}^2 + \hat{u}^2}{\hat{t}\hat{u}} [4(\hat{t}^2 + \hat{u}^2) - \hat{t}\hat{u}] \quad (\text{A.3c})$$

$$\overline{\sum} |\mathcal{A}(q\bar{q} \rightarrow Q\bar{Q}[^3P_0^{(8)}]g)|^2 = \frac{20(4\pi\alpha_s)^3}{81M^3} \frac{(\hat{s} - 3M^2)^2(\hat{t}^2 + \hat{u}^2)}{\hat{s}(\hat{s} - M^2)^4} \quad (\text{A.3d})$$

$$\overline{\sum_{h=0}} |\mathcal{A}(q\bar{q} \rightarrow Q\bar{Q}[^3P_1^{(8)}]g)|^2 = \frac{40(4\pi\alpha_s)^3}{81M^3} \frac{\hat{s}(\hat{t}^2 + \hat{u}^2)}{(\hat{s} - M^2)^4} \quad (\text{A.3e})$$

$$\overline{\sum_{|h|=1}} |\mathcal{A}(q\bar{q} \rightarrow Q\bar{Q}[^3P_1^{(8)}]g)|^2 = \frac{160(4\pi\alpha_s)^3}{81M^3} \frac{M^2\hat{t}\hat{u}}{(\hat{s} - M^2)^4} \quad (\text{A.3f})$$

$$\overline{\sum_{h=0}} |\mathcal{A}(q\bar{q} \rightarrow Q\bar{Q}[^3P_2^{(8)}]g)|^2 = \frac{8(4\pi\alpha_s)^3}{81M^3} \frac{\hat{s}(\hat{t}^2 + \hat{u}^2)}{(\hat{s} - M^2)^4} \quad (\text{A.3g})$$

$$\overline{\sum_{|h|=1}} |\mathcal{A}(q\bar{q} \rightarrow Q\bar{Q}[^3P_2^{(8)}]g)|^2 = \frac{32(4\pi\alpha_s)^3}{27M^3} \frac{M^2\hat{t}\hat{u}}{(\hat{s} - M^2)^4} \quad (\text{A.3h})$$

$$\overline{\sum_{|h|=2}} |\mathcal{A}(q\bar{q} \rightarrow Q\bar{Q}[^3P_2^{(8)}]g)|^2 = \frac{16(4\pi\alpha_s)^3}{27M^3} \frac{M^4(\hat{t}^2 + \hat{u}^2)}{\hat{s}(\hat{s} - M^2)^4} \quad (\text{A.3i})$$

$gq \rightarrow Q\bar{Q}[^{2s+1}L_J^{(8)}]q$  channel:

$$\overline{\sum} |\mathcal{A}(gq \rightarrow Q\bar{Q}[^1S_0^{(8)}]q)|^2 = -\frac{5(4\pi\alpha_s)^3}{72M} \frac{\hat{s}^2 + \hat{u}^2}{\hat{t}(\hat{t} - M^2)^2} \quad (\text{A.4a})$$

$$\overline{\sum_{h=0}} |\mathcal{A}(gq \rightarrow Q\bar{Q}[^3S_1^{(8)}]q)|^2 = -\frac{(4\pi\alpha_s)^3}{54M^3} \frac{M^2\hat{t}[4(\hat{s}^2 + \hat{u}^2) - \hat{s}\hat{u}]}{[(\hat{s} - M^2)(\hat{t} - M^2)]^2} \quad (\text{A.4b})$$

$$\begin{aligned} \overline{\sum_{|h|=1}} |\mathcal{A}(gq \rightarrow Q\bar{Q}[^3S_1^{(8)}]q)|^2 = & -\frac{(4\pi\alpha_s)^3}{108M^3} \frac{(\hat{s}^2 + \hat{u}^2 + 2M^2\hat{t})(\hat{s} - M^2)^2 - 2M^2\hat{s}\hat{t}\hat{u}}{\hat{s}\hat{u}[(\hat{s} - M^2)(\hat{t} - M^2)]^2} \\ & \times [4(\hat{s}^2 + \hat{u}^2) - \hat{s}\hat{u}] \end{aligned} \quad (\text{A.4c})$$

$$\overline{\sum} |\mathcal{A}(gq \rightarrow Q\bar{Q}[^3P_0^{(8)}]q)|^2 = -\frac{5(4\pi\alpha_s)^3}{54M^3} \frac{(\hat{t} - 3M^2)^2(\hat{s}^2 + \hat{u}^2)}{\hat{t}(\hat{t} - M^2)^4} \quad (\text{A.4d})$$

$$\overline{\sum_{h=0}} |\mathcal{A}(gq \rightarrow Q\bar{Q}[^3P_1^{(8)}]q)|^2 = -\frac{5(4\pi\alpha_s)^3}{27M^3} \frac{\hat{t}[\hat{s}^2(\hat{s} - M^2)^2 + \hat{u}^2(\hat{s} + M^2)^2]}{(\hat{t} - M^2)^4(\hat{s} - M^2)^2} \quad (\text{A.4e})$$

$$\overline{\sum_{|h|=1}} |\mathcal{A}(gq \rightarrow Q\bar{Q}[^3P_1^{(8)}]q)|^2 = -\frac{20(4\pi\alpha_s)^3}{27M^3} \frac{M^2\hat{s}\hat{u}(\hat{t}^2 + \hat{t}\hat{u} + \hat{u}^2)}{(\hat{t} - M^2)^4(\hat{s} - M^2)^2} \quad (\text{A.4f})$$

$$\begin{aligned} \overline{\sum_{h=0}} |\mathcal{A}(gq \rightarrow Q\bar{Q}[^3P_2^{(8)}]q)|^2 = & -\frac{(4\pi\alpha_s)^3}{27M^3} \frac{\hat{t}}{(\hat{t} - M^2)^4} \\ & \times [\hat{s}^2 + \hat{u}^2 + 12M^2\hat{s}\hat{u}^2 \frac{\hat{s}^2 + M^2\hat{s} + M^4}{(\hat{s} - M^2)^4}] \end{aligned} \quad (\text{A.4g})$$

$$\begin{aligned} \overline{\sum_{|h|=1}} |\mathcal{A}(gq \rightarrow Q\bar{Q}[^3P_2^{(8)}]q)|^2 = & -\frac{4(4\pi\alpha_s)^3}{9M^3} \frac{M^2\hat{s}\hat{u}}{(\hat{t} - M^2)^4} \\ & \times \frac{(\hat{s} - M^2)^2(\hat{s}^2 + M^4) - (\hat{s} + M^2)^2\hat{t}\hat{u}}{(\hat{s} - M^2)^4} \end{aligned} \quad (\text{A.4h})$$

$$\begin{aligned} \overline{\sum_{|h|=2}} |\mathcal{A}(gq \rightarrow Q\bar{Q}[^3P_2^{(8)}]q)|^2 = & -\frac{2(4\pi\alpha_s)^3}{9M^3} \frac{M^4}{\hat{t}(\hat{t} - M^2)^4} \\ & \times [\hat{s}^2 + \hat{u}^2 + 2\hat{s}^2\hat{t}\hat{u} \frac{(\hat{s} - M^2)(2\hat{t} + \hat{u}) - \hat{u}^2}{(\hat{s} - M^2)^4}] \end{aligned} \quad (\text{A.4i})$$

$gg \rightarrow Q\bar{Q}[{}^{2s+1}L_J^{(8)}]g$  channel: <sup>3</sup>

$$\begin{aligned} \overline{\sum} |\mathcal{A}(gg \rightarrow Q\bar{Q}[{}^1S_0^{(8)}]g)|^2 &= \frac{5(4\pi\alpha_s)^3}{16M} [\hat{s}^2(\hat{s} - M^2)^2 + \hat{s}\hat{t}\hat{u}(M^2 - 2\hat{s}) + (\hat{t}\hat{u})^2] \\ &\times \frac{(\hat{s}^2 - M^2\hat{s} + M^4)^2 - \hat{t}\hat{u}(2\hat{t}^2 + 3\hat{t}\hat{u} + 2\hat{u}^2)}{\hat{s}\hat{t}\hat{u}[(\hat{s} - M^2)(\hat{t} - M^2)(\hat{u} - M^2)]^2} \end{aligned} \quad (\text{A.5a})$$

$$\begin{aligned} \overline{\sum_{h=0}} |\mathcal{A}(gg \rightarrow Q\bar{Q}[{}^3S_1^{(8)}]g)|^2 &= -\frac{(4\pi\alpha_s)^3}{144M^3} \frac{2M^2\hat{s}}{(\hat{s} - M^2)^2} (\hat{t}^2 + \hat{u}^2)\hat{t}\hat{u} \\ &\times \frac{27(\hat{s}\hat{t} + \hat{t}\hat{u} + \hat{u}\hat{s}) - 19M^4}{[(\hat{s} - M^2)(\hat{t} - M^2)(\hat{u} - M^2)]^2} \end{aligned} \quad (\text{A.5b})$$

$$\begin{aligned} \overline{\sum_{|h|=1}} |\mathcal{A}(gg \rightarrow Q\bar{Q}[{}^3S_1^{(8)}]g)|^2 &= -\frac{(4\pi\alpha_s)^3}{144M^3} \frac{\hat{s}^2}{(\hat{s} - M^2)^2} [(\hat{s} - M^2)^4 + \hat{t}^4 + \hat{u}^4 + 2M^4(\frac{\hat{t}\hat{u}}{\hat{s}})^2] \\ &\times \frac{27(\hat{s}\hat{t} + \hat{t}\hat{u} + \hat{u}\hat{s}) - 19M^4}{[(\hat{s} - M^2)(\hat{t} - M^2)(\hat{u} - M^2)]^2} \end{aligned} \quad (\text{A.5c})$$

$$\begin{aligned} \overline{\sum} |\mathcal{A}(gg \rightarrow Q\bar{Q}[{}^3P_0^{(8)}]g)|^2 &= \frac{5(4\pi\alpha_s)^3}{12M^3} \\ &\times \left\{ \hat{s}^2\hat{z}^4(\hat{s}^2 - \hat{z}^2)^4 + M^2\hat{s}\hat{z}^2(\hat{s}^2 - \hat{z}^2)^2(3\hat{s}^2 - 2\hat{z}^2)(2\hat{s}^4 - 6\hat{s}^2\hat{z}^2 + 3\hat{z}^4) \right. \\ &+ M^4[9\hat{s}^{12} - 84\hat{s}^{10}\hat{z}^2 + 265\hat{s}^8\hat{z}^4 - 382\hat{s}^6\hat{z}^6 + 276\hat{s}^4\hat{z}^8 - 88\hat{s}^2\hat{z}^{10} + 9\hat{z}^{12}] \\ &- M^6\hat{s}[54\hat{s}^{10} - 357\hat{s}^8\hat{z}^2 + 844\hat{s}^6\hat{z}^4 - 898\hat{s}^4\hat{z}^6 + 439\hat{s}^2\hat{z}^8 - 81\hat{z}^{10}] \\ &+ M^8[153\hat{s}^{10} - 798\hat{s}^8\hat{z}^2 + 1415\hat{s}^6\hat{z}^4 - 1041\hat{s}^4\hat{z}^6 + 301\hat{s}^2\hat{z}^8 - 18\hat{z}^{10}] \\ &- M^{10}\hat{s}[270\hat{s}^8 - 1089\hat{s}^6\hat{z}^2 + 1365\hat{s}^4\hat{z}^4 - 616\hat{s}^2\hat{z}^6 + 87\hat{z}^8] \\ &+ M^{12}[324\hat{s}^8 - 951\hat{s}^6\hat{z}^2 + 769\hat{s}^4\hat{z}^4 - 189\hat{s}^2\hat{z}^6 + 9\hat{z}^8] \\ &- 9M^{14}\hat{s}(6\hat{s}^2 - \hat{z}^2)(5\hat{s}^4 - 9\hat{s}^2\hat{z}^2 + 3\hat{z}^4) \\ &+ 3M^{16}\hat{s}^2(51\hat{s}^4 - 59\hat{s}^2\hat{z}^2 + 12\hat{z}^4) - 27M^{18}\hat{s}^3(2\hat{s}^2 - \hat{z}^2) + 9M^{20}\hat{s}^4 \Big\} \\ &/ [\hat{s}\hat{z}^2(\hat{s} - M^2)^4(\hat{s}M^2 + \hat{z}^2)^4] \end{aligned} \quad (\text{A.5d})$$

---

<sup>3</sup> The  $gg \rightarrow Q\bar{Q}[{}^3P_J^{(8)}]g$  squared amplitudes are expressed in terms of the variables  $\hat{s}$  and  $\hat{z} \equiv \sqrt{\hat{t}\hat{u}}$ .

$$\begin{aligned}
\overline{\sum_{h=0}} |\mathcal{A}(gg \rightarrow Q\overline{Q}[{}^3P_1^{(8)}]g)|^2 &= \frac{5(4\pi\alpha_s)^3}{6M^3} \\
&\times \hat{s}\hat{z}^2 [(\hat{s}^2 - \hat{z}^2)^2 - 2M^2\hat{s}\hat{z}^2 - M^4(\hat{s}^2 + 2\hat{z}^2) + M^8] \\
&\times [(\hat{s}^2 - \hat{z}^2)^2 - M^2\hat{s}(2\hat{s}^2 - \hat{z}^2) + M^4\hat{s}^2] / [(\hat{s} - M^2)^4(\hat{s}M^2 + \hat{z}^2)^4] \quad (\text{A.5e})
\end{aligned}$$

$$\begin{aligned}
\overline{\sum_{|h|=1}} |\mathcal{A}(gg \rightarrow Q\overline{Q}[{}^3P_1^{(8)}]g)|^2 &= \frac{5(4\pi\alpha_s)^3}{6M^3} \\
&\times M^2 \left\{ 2(\hat{s}^2 - \hat{z}^2)^2(\hat{s}^6 - 4\hat{s}^4\hat{z}^2 + \hat{s}^2\hat{z}^4 - \hat{z}^6) \right. \\
&\quad - M^2\hat{s}(2\hat{s}^2 - \hat{z}^2)(5\hat{s}^6 - 17\hat{s}^4\hat{z}^2 + 9\hat{s}^2\hat{z}^4 - \hat{z}^6) \\
&\quad + M^4(21\hat{s}^8 - 49\hat{s}^6\hat{z}^2 + 21\hat{s}^4\hat{z}^4 - 4\hat{s}^2\hat{z}^6 + \hat{z}^8) \\
&\quad - M^6\hat{s}(24\hat{s}^6 - 30\hat{s}^4\hat{z}^2 + 6\hat{s}^2\hat{z}^4 - \hat{z}^6) \\
&\quad \left. + M^8\hat{s}^2(16\hat{s}^4 - 9\hat{s}^2\hat{z}^2 + 2\hat{z}^4) - M^{10}\hat{s}^3(6\hat{s}^2 - \hat{z}^2) + M^{12}\hat{s}^4 \right\} \\
&/ [(\hat{s} - M^2)^4(\hat{s}M^2 + \hat{z}^2)^4] \quad (\text{A.5f})
\end{aligned}$$

$$\begin{aligned}
\overline{\sum_{h=0}} |\mathcal{A}(gg \rightarrow Q\overline{Q}[{}^3P_2^{(8)}]g)|^2 &= \frac{(4\pi\alpha_s)^3}{6M^3} \\
&\times \hat{s}\hat{z}^2 \left\{ \hat{s}^2(\hat{s}^2 - \hat{z}^2)^4 - M^2\hat{s}\hat{z}^2(\hat{s}^2 - \hat{z}^2)^2(11\hat{s}^2 + 2\hat{z}^2) \right. \\
&\quad + M^4[\hat{s}^8 - 12\hat{s}^6\hat{z}^2 + 41\hat{s}^4\hat{z}^4 - 20\hat{s}^2\hat{z}^6 + \hat{z}^8] \\
&\quad - M^6\hat{s}[4\hat{s}^6 - 26\hat{s}^4\hat{z}^2 - \hat{s}^2\hat{z}^4 - 5\hat{z}^6] \\
&\quad + M^8[29\hat{s}^6 - 114\hat{s}^4\hat{z}^2 + 108\hat{s}^2\hat{z}^4 - 10\hat{z}^6] \\
&\quad - M^{10}\hat{s}[65\hat{s}^4 - 104\hat{s}^2\hat{z}^2 - 33\hat{z}^4] + M^{12}[54\hat{s}^4 - 20\hat{s}^2\hat{z}^2 + 7\hat{z}^4] \\
&\quad \left. - M^{14}\hat{s}(23\hat{s}^2 + 5\hat{z}^2) + 7M^{16}\hat{s}^2 \right\} / [(\hat{s} - M^2)^6(\hat{s}M^2 + \hat{z}^2)^4] \quad (\text{A.5g})
\end{aligned}$$

$$\begin{aligned}
& \overline{\sum_{|h|=1}} |\mathcal{A}(gg \rightarrow Q\overline{Q}[{}^3P_2^{(8)}]g)|^2 = \frac{(4\pi\alpha_s)^3}{2M^3} \\
& \times M^2 \left\{ 2\hat{s}^2(\hat{s}^2 - \hat{z}^2)^2(\hat{s}^6 - 4\hat{s}^4\hat{z}^2 + \hat{s}^2\hat{z}^4 - \hat{z}^6) \right. \\
& - M^2\hat{s}[10\hat{s}^{10} - 37\hat{s}^8\hat{z}^2 + 19\hat{s}^6\hat{z}^4 + 11\hat{s}^4\hat{z}^6 - \hat{s}^2\hat{z}^8 - 4\hat{z}^{10}] \\
& + M^4[25\hat{s}^{10} - 61\hat{s}^8\hat{z}^2 + 27\hat{s}^6\hat{z}^4 - 34\hat{s}^4\hat{z}^6 + 23\hat{s}^2\hat{z}^8 - 2\hat{z}^{10}] \\
& - M^6\hat{s}[42\hat{s}^8 - 77\hat{s}^6\hat{z}^2 + 41\hat{s}^4\hat{z}^4 - 22\hat{s}^2\hat{z}^6 + 17\hat{z}^8] \\
& + M^8[53\hat{s}^8 - 88\hat{s}^6\hat{z}^2 + 69\hat{s}^4\hat{z}^4 - 68\hat{s}^2\hat{z}^6 + 3\hat{z}^8] \\
& - M^{10}\hat{s}[54\hat{s}^6 - 85\hat{s}^4\hat{z}^2 + 60\hat{s}^2\hat{z}^4 - 9\hat{z}^6] + M^{12}\hat{s}^2[43\hat{s}^4 - 47\hat{s}^2\hat{z}^2 + 20\hat{z}^4] \\
& \left. - M^{14}\hat{s}^3(22\hat{s}^2 - 9\hat{z}^2) + 5M^{16}\hat{s}^4 \right\} / [(\hat{s} - M^2)^6(\hat{s}M^2 + \hat{z}^2)^4] \quad (A.5h)
\end{aligned}$$

$$\begin{aligned}
& \overline{\sum_{|h|=2}} |\mathcal{A}(gg \rightarrow Q\overline{Q}[{}^3P_2^{(8)}]g)|^2 = \frac{(4\pi\alpha_s)^3}{2M^3} \\
& \times M^4 \left\{ 2\hat{s}^2[\hat{s}^{12} - 8\hat{s}^{10}\hat{z}^2 + 22\hat{s}^8\hat{z}^4 - 24\hat{s}^6\hat{z}^6 + 10\hat{s}^4\hat{z}^8 - 3\hat{s}^2\hat{z}^{10} + \hat{z}^{12}] \right. \\
& - M^2\hat{s}[16\hat{s}^{12} - 102\hat{s}^{10}\hat{z}^2 + 210\hat{s}^8\hat{z}^4 - 153\hat{s}^6\hat{z}^6 + 36\hat{s}^4\hat{z}^8 - 6\hat{s}^2\hat{z}^{10} + 4\hat{z}^{12}] \\
& + M^4[60\hat{s}^{12} - 306\hat{s}^{10}\hat{z}^2 + 482\hat{s}^8\hat{z}^4 - 271\hat{s}^6\hat{z}^6 + 77\hat{s}^4\hat{z}^8 - 18\hat{s}^2\hat{z}^{10} + 2\hat{z}^{12}] \\
& - M^6\hat{s}[140\hat{s}^{10} - 573\hat{s}^8\hat{z}^2 + 710\hat{s}^6\hat{z}^4 - 344\hat{s}^4\hat{z}^6 + 91\hat{s}^2\hat{z}^8 - 18\hat{z}^{10}] \\
& + M^8[226\hat{s}^{10} - 741\hat{s}^8\hat{z}^2 + 737\hat{s}^6\hat{z}^4 - 310\hat{s}^4\hat{z}^6 + 77\hat{s}^2\hat{z}^8 - 4\hat{z}^{10}] \\
& - M^{10}\hat{s}[264\hat{s}^8 - 686\hat{s}^6\hat{z}^2 + 541\hat{s}^4\hat{z}^4 - 177\hat{s}^2\hat{z}^6 + 25\hat{z}^8] \\
& + M^{12}[226\hat{s}^8 - 452\hat{s}^6\hat{z}^2 + 261\hat{s}^4\hat{z}^4 - 55\hat{s}^2\hat{z}^6 + 2\hat{z}^8] \\
& - M^{14}\hat{s}[140\hat{s}^6 - 201\hat{s}^4\hat{z}^2 + 71\hat{s}^2\hat{z}^4 - 6\hat{z}^6] \\
& \left. + M^{16}\hat{s}^2[60\hat{s}^4 - 53\hat{s}^2\hat{z}^2 + 8\hat{z}^4] - 2M^{18}\hat{s}^3[8\hat{s}^2 - 3\hat{z}^2] + 2M^{20}\hat{s}^4 \right\} \\
& / [\hat{s}\hat{z}^2(\hat{s} - M^2)^6(\hat{s}M^2 + \hat{z}^2)^4] \quad (A.5i)
\end{aligned}$$

## Figure Captions

Fig. 1. Lowest order Feynman graph which mediates  $q + \bar{q} \rightarrow Q + \bar{Q}$  scattering.

Fig. 2. Lowest order Feynman graphs which mediate  $g + g \rightarrow Q + \bar{Q}$  scattering.

Fig. 3. Feynman diagrams which mediate (a)  $q\bar{q} \rightarrow \psi_Q g$ , (b)  $gq \rightarrow \psi_Q q$  and (c)  $gg \rightarrow \psi_Q g$  scattering through intermediate  $Q\bar{Q}[{}^3P_J^{(8)}]$  and  $Q\bar{Q}[{}^1S_0^{(8)}]$  pairs.

Fig. 4. Ratio  $R(p_\perp)$  of the total  $Q\bar{Q}[{}^3P_J^{(8)}]$  and  $Q\bar{Q}[{}^1S_0^{(8)}]$  contributions to the  $\psi_Q$  transverse momentum differential cross section in the limit where the long distance NRQCD matrix element  $\langle \mathcal{O}_8^{\psi_Q}({}^3P_0) \rangle$  equals  $M_Q^2 \langle \mathcal{O}_8^{\psi_Q}({}^1S_0) \rangle$ . The solid and dotted curves illustrate  $R(p_\perp)$  for the charmonia and bottomonia sectors respectively.

Fig. 5. Theoretical transverse momentum differential cross section for prompt  $\psi'$  production at the Tevatron in the pseudorapidity interval  $|\eta| \leq 0.6$  compared against preliminary CDF data. The dashed curve depicts the direct color-singlet contribution to  $\psi'$  production. The dot-dashed curve illustrates the  $c\bar{c}[{}^3S_1^{(8)}]$  cross section, and the dotted curve denotes the combined  $c\bar{c}[{}^3P_J^{(8)}]$  and  $c\bar{c}[{}^1S_0^{(8)}]$  distributions. The solid curve equals the sum of the color-singlet and color-octet contributions and represents the total theoretical prediction for the  $\psi'$  differential cross section. All curves are multiplied by the muon branching fraction  $\text{Br}(\psi' \rightarrow \mu^+ \mu^-)$ .

Fig. 6. Theoretical transverse momentum differential cross section for prompt  $J/\psi$  production at the Tevatron in the pseudorapidity interval  $|\eta| \leq 0.6$  compared against preliminary CDF data. The curves in this figure are labeled in the same way as those in fig. 5. All curves are multiplied by the muon branching fraction  $\text{Br}(J/\psi \rightarrow \mu^+ \mu^-)$ .

Fig. 7. Theoretical transverse momentum differential cross section for  $J/\psi$  production at the Tevatron in the pseudorapidity interval  $|\eta| \leq 0.6$  resulting from radiative  $\chi_{cJ}$  decay compared against preliminary CDF data. The dashed curve depicts the color-singlet contribution, the dot-dashed curve illustrates the  $c\bar{c}[{}^3S_1^{(8)}]$  cross section and the solid curve represents their sum. All curves are multiplied by the muon branching fraction  $\text{Br}(J/\psi \rightarrow \mu^+ \mu^-)$ .

Fig. 8. Theoretical transverse momentum differential cross section for  $\Upsilon(1S)$  production at the Tevatron in the rapidity interval  $|y| \leq 0.4$  compared against preliminary CDF data. The dashed curve depicts the color-singlet contribution which includes direct  $\Upsilon(1S)$  production as well as radiative feeddown from  $\chi_{bJ}(1P)$  and  $\chi_{bJ}(2P)$  states. The dot-dashed curve illustrates the  $b\bar{b}[{}^3S_1^{(8)}]$  cross section, and the dotted curve denotes the combined  $b\bar{b}[{}^3P_J^{(8)}]$  and  $b\bar{b}[{}^1S_0^{(8)}]$  distributions. The solid curve equals the sum of the color-singlet and color-octet contributions and represents

the total theoretical prediction for the  $\Upsilon(1S)$  differential cross section. All curves are multiplied by the muon branching fraction  $\text{Br}(\Upsilon(1S) \rightarrow \mu^+ \mu^-)$ .

Fig. 9. Theoretical transverse momentum differential cross section for  $\Upsilon(2S)$  production at the Tevatron in the rapidity interval  $|y| \leq 0.4$  compared against preliminary CDF data. The curves in this figure are labeled the same as those in fig. 8. The dashed color-singlet cross section includes  $\Upsilon(2S)$  production and radiative feeddown from  $\chi_{bJ}(2P)$ . All curves are multiplied by the muon branching fraction  $\text{Br}(\Upsilon(2S) \rightarrow \mu^+ \mu^-)$ .

## References

- [1] G.T. Bodwin, E. Braaten and G.P. Lepage, Phys. Rev. **D51** (1995) 1125.
- [2] G.P. Lepage, L. Magnea, C. Nakhleh, U. Magnea and K. Hornbostel, Phys. Rev. **D46** (1992) 4052.
- [3] C.H. Chang, Nucl. Phys. **B172** (1980) 425.
- [4] E.L. Berger and D. Jones, Phys. Rev. **D23** (1981) 1521.
- [5] J. H. Kühn, J. Kaplan and E. G. O. Safiani, Nucl. Phys. **B157** (1979) 125.
- [6] B. Guberina, J.H. Kühn, R.D. Peccei and R. Rückl, Nucl. Phys. **B174** (1980) 317.
- [7] R. Baier and R. Rückl, Z. Phys. C **19** (1983) 251.
- [8] P. Cho and A.K. Leibovich, Phys. Rev. **D53** (1996) 150.
- [9] W.-K. Tang and M. Vänttinien, SLAC-PUB-95-6931 (1995), unpublished.
- [10] The CDF collaboration, Fermilab-Conf-94/136-E (1994), unpublished.
- [11] The CDF collaboration, Fermilab-conf-95/128-E (1995), unpublished.
- [12] The CDF collaboration, Fermilab-Pub-95/271-E (1995), unpublished.
- [13] E.J. Eichten and C. Quigg, Phys. Rev. **D52** (1995) 1726.
- [14] R. Mertig, M. Böhm and A. Denner, Comp. Phys. Comm. **64** (1991) 345.
- [15] E. Braaten and T.C. Yuan, Phys. Rev. Lett. **71** (1993) 1673.
- [16] E. Braaten and T.C. Yuan, Phys. Rev. **D50** (1994) 3176.
- [17] E. Braaten, M.A. Doncheski, S. Fleming and M.L. Mangano, Phys. Lett. **B333** (1994) 548.
- [18] D.P. Roy and K. Sridhar, Phys. Lett. **B339** (1994) 141.
- [19] M. Cacciari and M. Greco, Phys. Rev. Lett. **73** (1994) 1586.
- [20] E. Braaten and S. Fleming, Phys. Rev. Lett. **74** (1995) 3327.
- [21] M. Cacciari, M. Greco, M.L. Mangano and A. Petrelli, Phys. Lett. **B356** (1995), 553.
- [22] The UA1 collaboration, Phys. Lett. **B256** (1991) 112.
- [23] K. Cheung, W.-Y. Keung and T.C. Yuan, Phys. Rev. Lett. **76** (1996) 877.
- [24] P. Cho, Phys. Lett. **B368** (1996) 171.
- [25] E. Braaten and Y.-Q. Chen, Phys. Rev. Lett. **76** (1996) 730.
- [26] P. Ko, J. Lee and H.S. Song, Phys. Rev. **D53** (1996) 1409.
- [27] M. Beneke and I.Z. Rothstein, SLAC-PUB-7129 (1996), unpublished.
- [28] E. Braaten and Y.-Q. Chen, OHSTPY-HEP-T-96-010 (1996), unpublished.

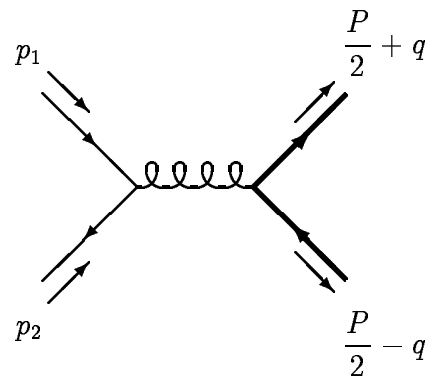


Figure 1

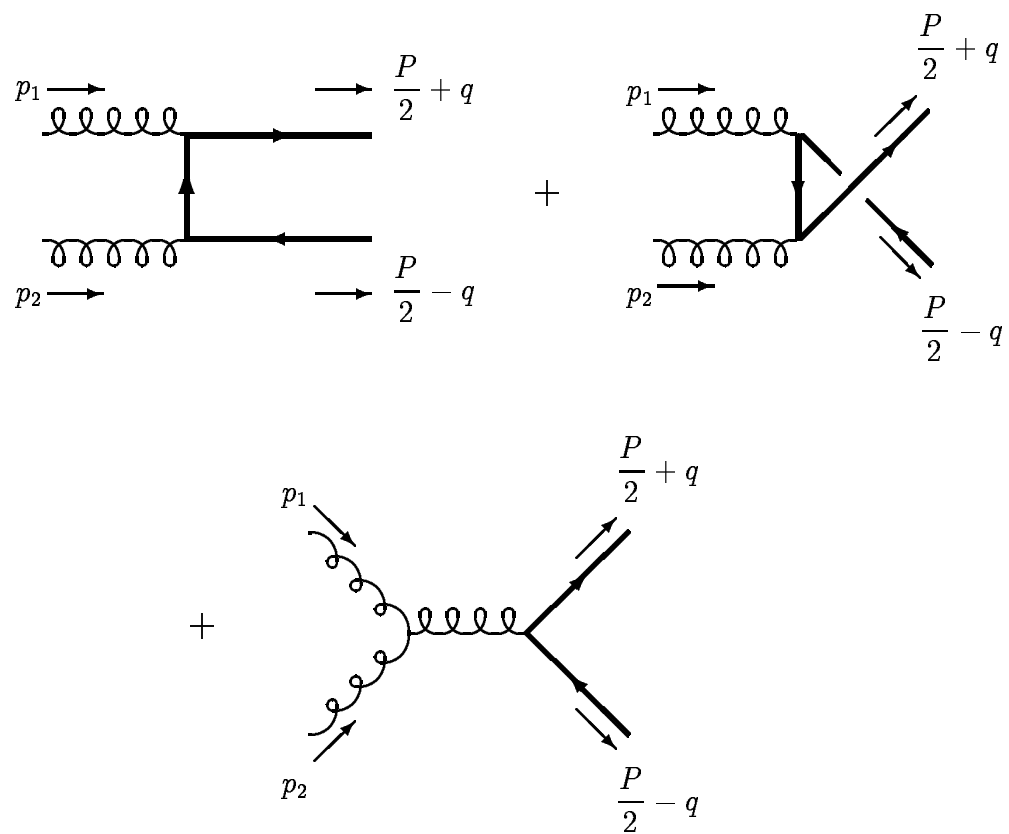


Figure 2

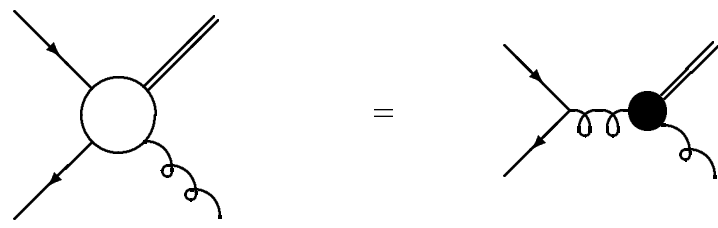


Figure 3a

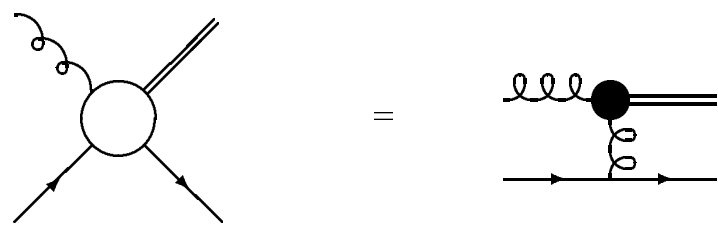


Figure 3b

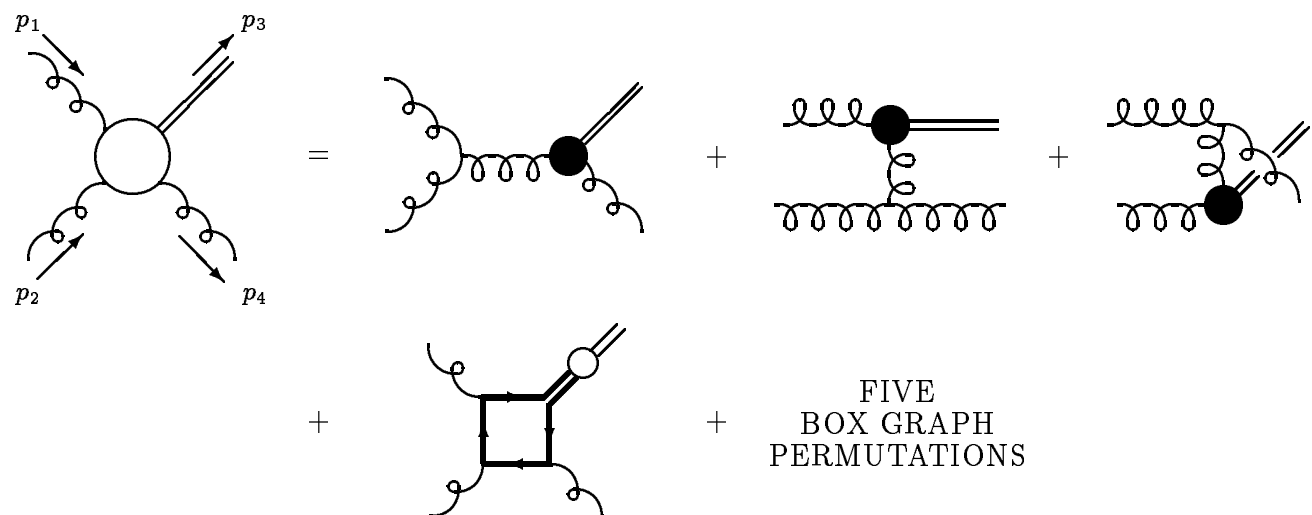


Figure 3c

$R(p_\perp)$

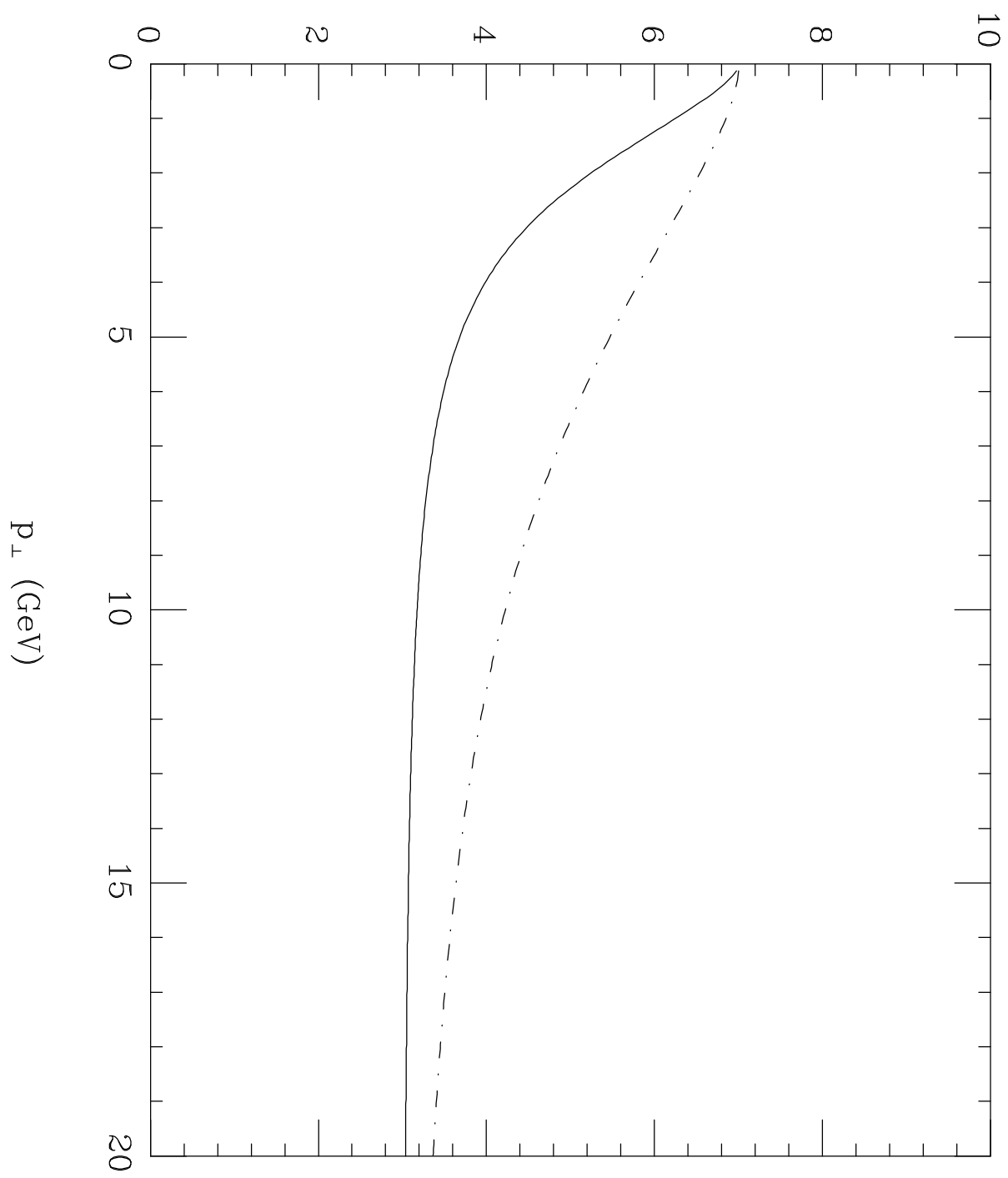


Figure 4

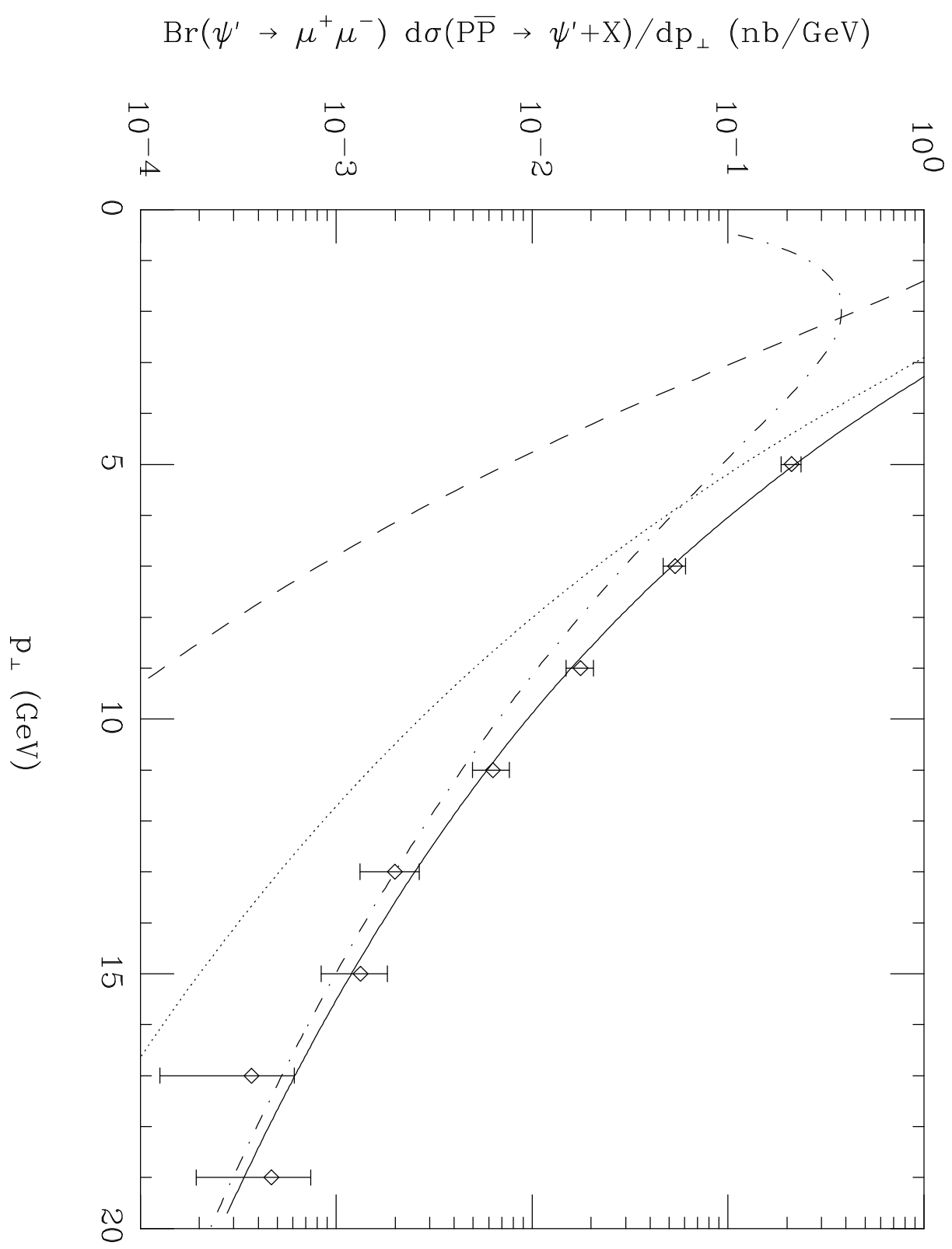


Figure 5

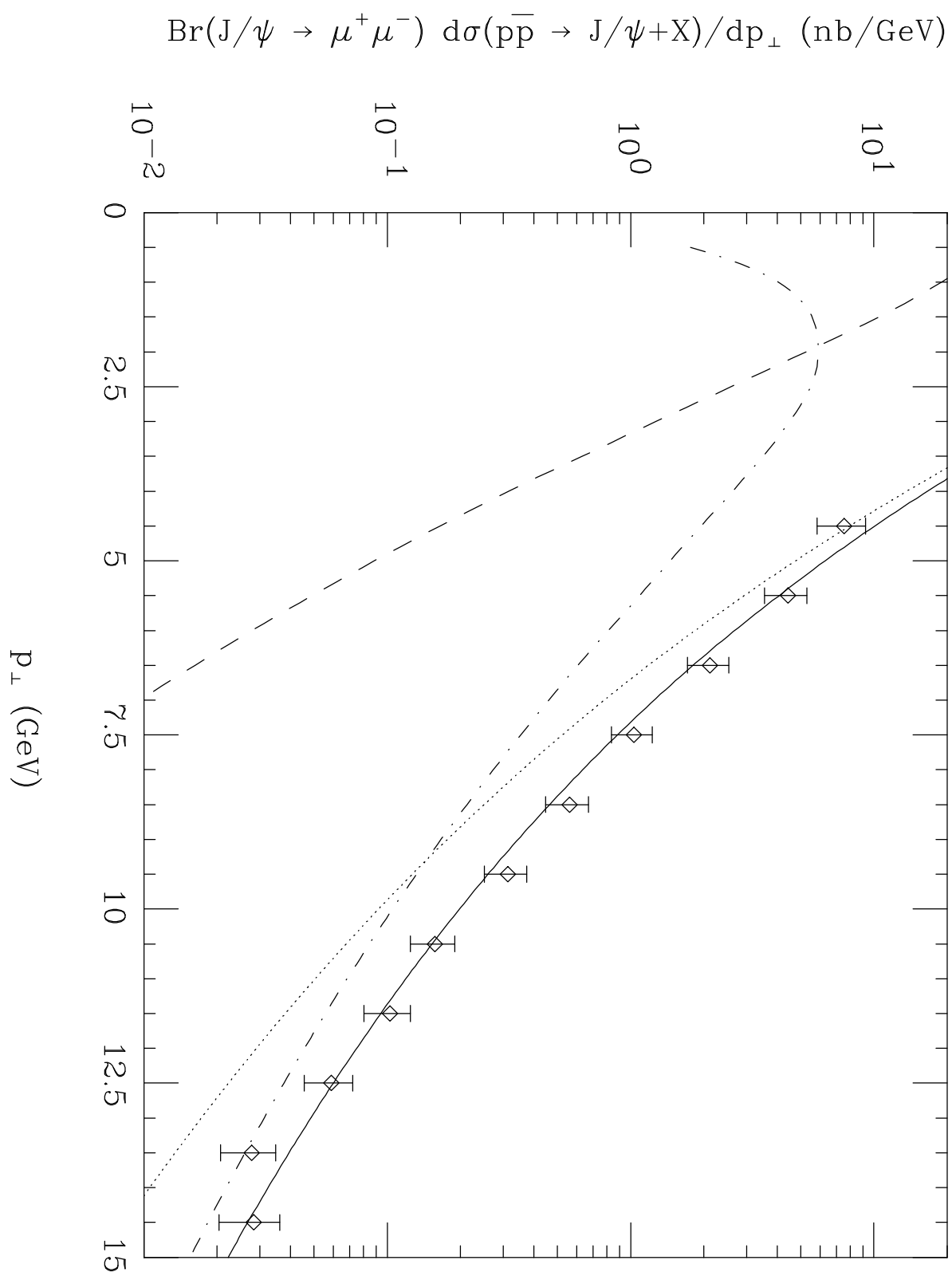


Figure 6

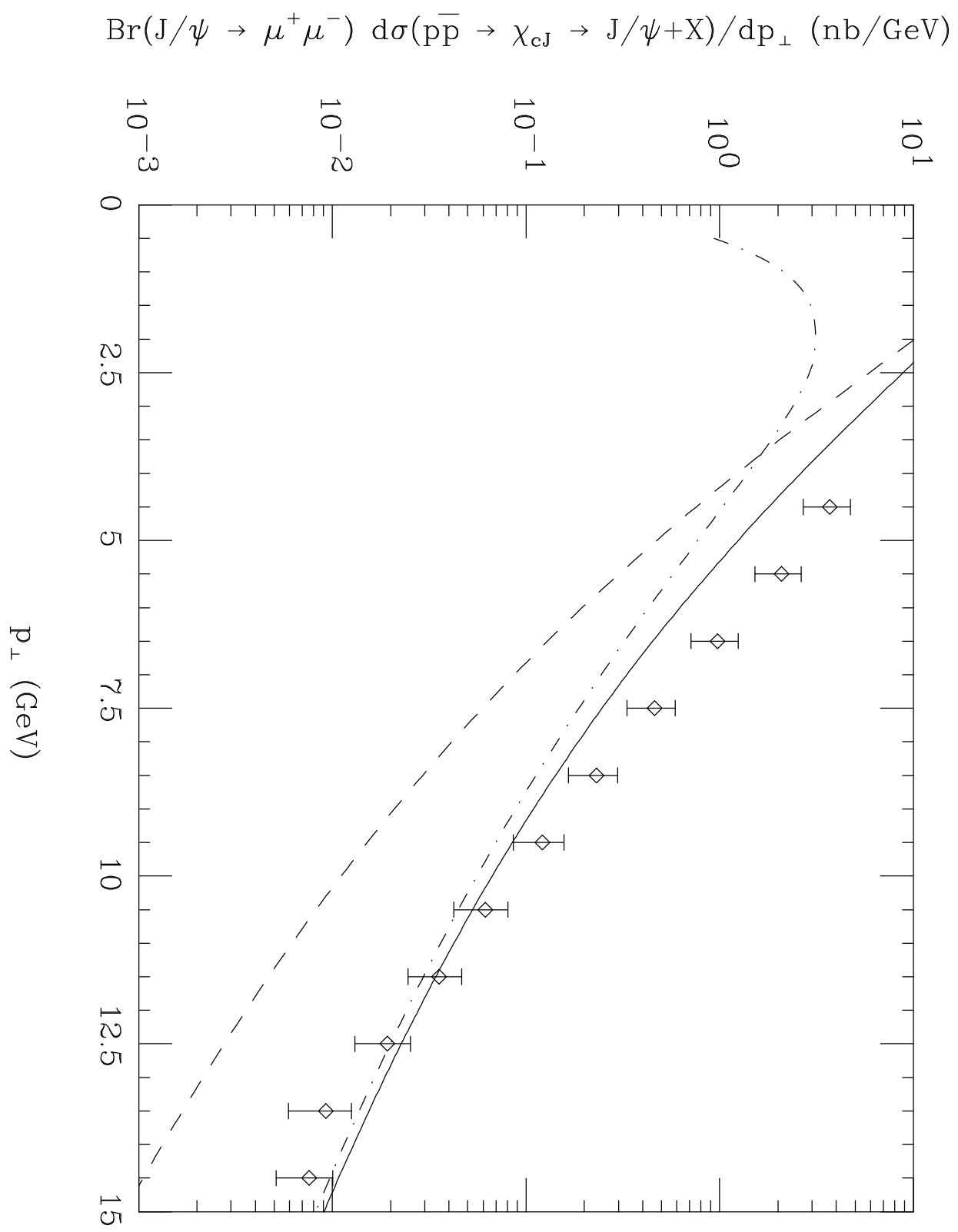


Figure 7

$\text{Br}(\Upsilon(1S) \rightarrow \mu^+ \mu^-) \text{ d}\sigma(p\bar{p} \rightarrow \Upsilon(1S) + X) / \text{d}p_\perp \text{ (nb/GeV)}$

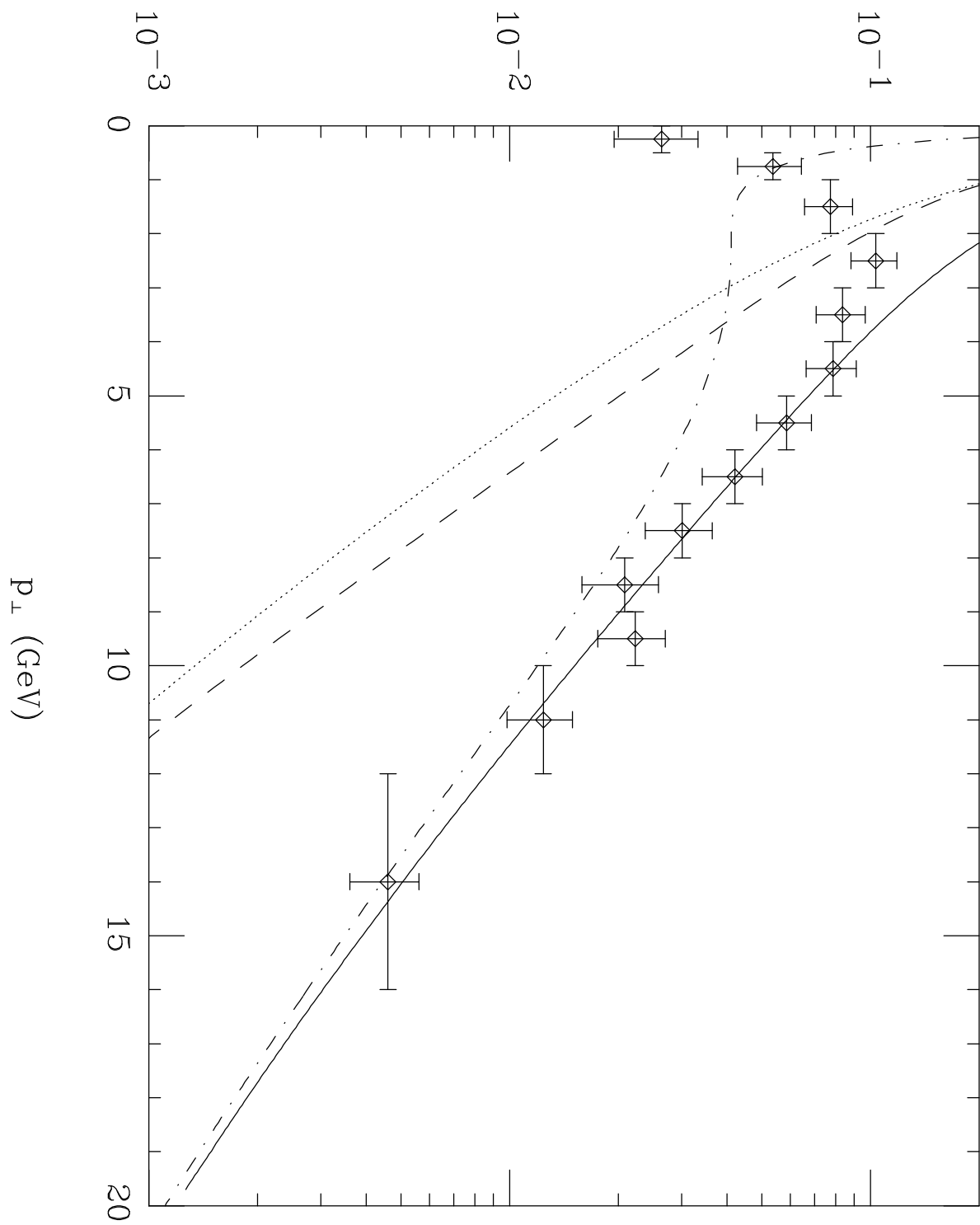


Figure 8

$\text{Br}(\Upsilon(2S) \rightarrow \mu^+ \mu^-) \text{ d}\sigma(p\bar{p} \rightarrow \Upsilon(2S) + X)/\text{d}p_\perp \text{ (nb/GeV)}$

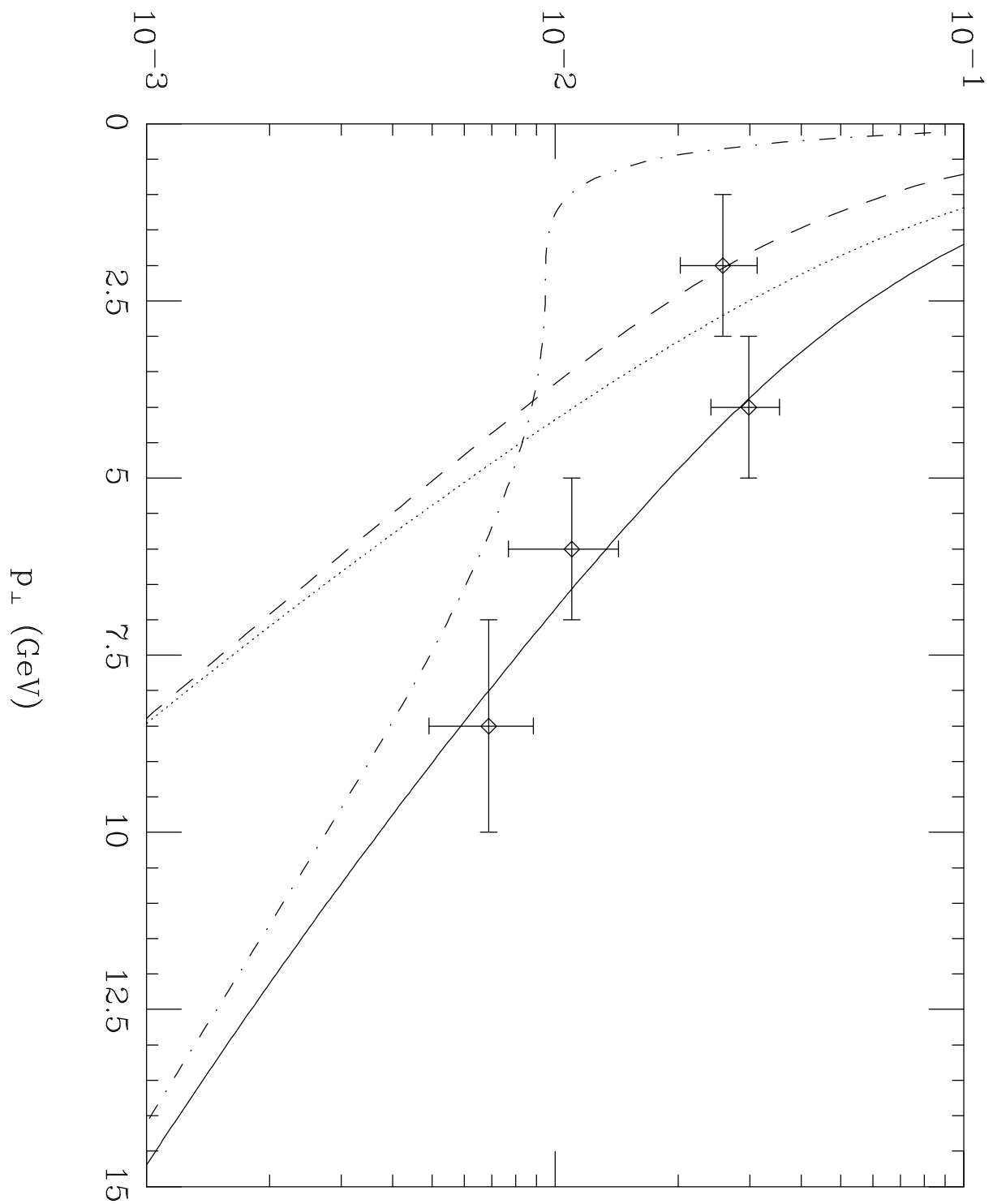


Figure 9